

AD-A272 505



2

# NAVAL POSTGRADUATE SCHOOL Monterey, California



DTIC  
ELECTE  
NOV 05 1993  
S B D

## THESIS

Validation of the Design of a High Resolution  
All-Reflection Michelson Interferometer for Atmospheric Spectroscopy

by

Scott M. Carlson

June 1993

Thesis Advisor:

David D. Cleary

Approved for public release; distribution is unlimited

93-27046



SS

# REPORT DOCUMENTATION PAGE

Form Approved  
OMB No. 0704-0188

Public reporting burden for this collection of information is estimated to average 1 hour per response, including the time for reviewing instructions, searching existing data sources, gathering and maintaining the data needed, and completing and reviewing the collection of information. Send comments regarding this burden estimate or any other aspect of this collection of information, including suggestions for reducing this burden, to Washington Headquarters Services, Directorate for Information Operations and Reports, 1215 Jefferson Davis Highway, Suite 1204, Arlington, VA 22202-4302 and to the Office of Management and Budget, Paperwork Reduction Project (0704-0188), Washington, DC 20503

<b>1. AGENCY USE ONLY (Leave blank)</b>		<b>2. REPORT DATE</b> JUN 93	<b>3. REPORT TYPE AND DATES COVERED</b> Master's Thesis	
<b>4. TITLE AND SUBTITLE</b> Validation of the Design of a High Resolution All-Reflection Michelson Interferometer for Atmospheric Spectroscopy			<b>5. FUNDING NUMBERS</b>	
<b>6. AUTHOR(S)</b> Carlson, Scott M.				
<b>7. PERFORMING ORGANIZATION NAME(S) AND ADDRESS(ES)</b> Naval Postgraduate School Monterey, CA 93943-5000			<b>8. PERFORMING ORGANIZATION REPORT NUMBER</b>	
<b>9. SPONSORING/MONITORING AGENCY NAME(S) AND ADDRESS(ES)</b> Naval Postgraduate School Monterey, CA 93943-5000			<b>10. SPONSORING/MONITORING AGENCY REPORT NUMBER</b>	
<b>11. SUPPLEMENTARY NOTES</b> The views expressed in this thesis are those of the author and do not reflect the official policy or position of the Department of Defense or the U.S. Government.				
<b>12a. DISTRIBUTION/AVAILABILITY STATEMENT</b> Approved for public release; distribution is unlimited.			<b>12b. DISTRIBUTION CODE</b>	
<b>13. ABSTRACT (Maximum 200 words)</b> The design of a high resolution Plane Grating All-reflection Michelson Interferometer for ionospheric spectroscopy was analyzed using ray tracing techniques. This interferometer produces an interference pattern whose spatial frequency is wavelength dependent. The instrument is intended for remote observations of the atomic oxygen triplet emission line profile at 1304 Å in the thermosphere from sounding rocket or satellite platforms. The device was modeled using the PC-based ray tracing application, DART, and results analyzed through fourier techniques using the PC with Windows version of the Interactive Data Language (IDL). Through these methods, instrument resolution, resolving power, and bandpass were determined. An analysis of the effects of aperture size and shape on instrument performance was also conducted.				
<b>14. SUBJECT TERMS</b> Spectroscopy, Interferometer, Michelson Interferometer.			<b>15. NUMBER OF PAGES</b> 86	
			<b>16. PRICE CODE</b>	
<b>17. SECURITY CLASSIFICATION OF REPORT</b> UNCLASSIFIED	<b>18. SECURITY CLASSIFICATION OF THIS PAGE</b> UNCLASSIFIED	<b>19. SECURITY CLASSIFICATION OF ABSTRACT</b> UNCLASSIFIED	<b>20. LIMITATION OF ABSTRACT</b> SAR	

Approved for public release; distribution is unlimited

**Validation of the Design of a High Resolution  
All-Reflection Michelson Interferometer for Atmospheric Spectroscopy**

by

**Scott M. Carlson  
Lieutenant, United States Navy  
B.S.S.E., United States Naval Academy, 1985**

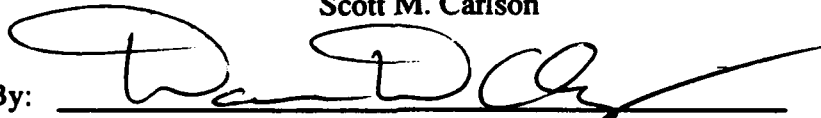
Submitted in partial fulfillment of the requirements for the degree of

**MASTER OF SCIENCE IN PHYSICS**

from the

**NAVAL POSTGRADUATE SCHOOL  
June 1993**

Author:   
\_\_\_\_\_  
Scott M. Carlson

Approved By:   
\_\_\_\_\_  
David D. Cleary, Thesis Advisor

  
\_\_\_\_\_  
Suntharalingam Gnanalingam, Second Reader

  
\_\_\_\_\_  
Karlheinz E. Woehler, Chairman, Department of Physics

## ABSTRACT

The design of a high resolution Plane Grating All-reflection Michelson Interferometer for ionospheric spectroscopy was analyzed using ray tracing techniques. This interferometer produces an interference pattern whose spatial frequency is wavelength dependent. The instrument is intended for remote observations of the atomic oxygen triplet emission line profile at 1304 Å in the thermosphere from sounding rocket or satellite platforms. The device was modeled using the PC-based ray tracing application, DART, and results analyzed through fourier techniques using the PC with Windows version of the Interactive Data Language (IDL). Through these methods, instrument resolution, resolving power, and bandpass were determined. An analysis of the effects of aperture size and shape on instrument performance was also conducted.

DTIC TAB

<b>Accession For</b>	
NTIS GRA&I	<input checked="" type="checkbox"/>
DTIC TAB	<input type="checkbox"/>
Unannounced	<input type="checkbox"/>
Justification	
By _____	
Distribution/	
Availability Codes	
Dist	Avail and/or Special
A-1	

## TABLE OF CONTENTS

I.	INTRODUCTION .....	1
	A. THESIS OBJECTIVES .....	2
	B. THESIS OUTLINE.....	2
II.	BACKGROUND .....	3
	A. ATMOSPHERIC COMPOSITION .....	3
	B. MOTIVATION FOR STUDY .....	5
	1. Naval Postgraduate School Research.....	5
	2. Motivation for High Resolution Spectroscopy .....	5
III.	THEORY .....	7
	A. SOLAR OXYGEN 1304 Å TRIPLET LINE PROFILE .....	7
	B. INTERFERENCE AND DIFFRACTION .....	9
	1. Interference Theory.....	10
	2. Diffraction Theory .....	13
	C. THE ALL-REFLECTION MICHELSON INTERFEROMETER .....	15
IV.	RAY TRACING PROCEDURES .....	21
	A. DART RAY TRACING PROGRAM.....	21
	B. RAY TRACING SOFTWARE LIMITATIONS .....	23
V.	EXPERIMENTAL PROCEDURE AND RESULTS .....	25
	A. IDL FOURIER TRANSFORM PROCEDURES .....	25
	B. EXPERIMENT DOCUMENTATION .....	26
	C. RAY TRACING PROGRAM SETUP .....	27
	1. Interferometer .....	27

2. Off-axis Parabolic Reflector .....	31
3. All-Reflection Michelson Interferometer .....	32
D. AMI MODEL VALIDATION AND OPTIMIZATION .....	34
1. Ideal Point Source with Monochromatic Incident Light.....	35
2. Ideal Point Source with a Multiple Wavelength Light Source .....	43
3. Offset Ideal Point Source .....	48
4. Pinhole Source .....	49
5. Slit Source .....	53
6. Other Results.....	53
E. OXYGEN 1304 Å LINE PROFILE INTERFERENCE.....	53
1. Profile Modeling .....	53
2. 1304 Å Line Profile Interference Results .....	54
F. RESULTS SUMMARY.....	59
VI. CONCLUSIONS AND RECOMMENDATIONS .....	62
A. SUMMARY OF FINDINGS AND CONCLUSIONS .....	62
B. RECOMMENDATIONS FOR FURTHER STUDY.....	63
APPENDIX A.....	65
APPENDIX B .....	71
LIST OF REFERENCES.....	78
INITIAL DISTRIBUTION LIST .....	79

## I. INTRODUCTION

Knowledge of the makeup of the Earth's atmosphere is an area of intense academic and government interest. Specifically, the Department of Defense (DoD) has a stated requirement to gain an understanding of the electron density profile of the ionosphere for applications in over-the-horizon RADAR and long-range communications. Knowledge of the altitude distribution of atomic oxygen is of interest to the scientific community because atomic oxygen density is known to be an important component of photochemical models of the atmosphere. Additionally, DoD and NASA have become concerned with the material degradation of spacecraft surfaces exposed to atomic oxygen in flight. In each application, accurate measurement of the altitude distribution of atomic oxygen is a requirement.

The most common method for studying the upper atmosphere has been through the use of experimental sounding rockets. Additional information has been gained through extensive study of the propagation of electromagnetic waves in the ionosphere. The Naval Postgraduate School Physics Department, through the efforts of the Center for Space Systems Applications, has been involved in ionospheric research for several years. They have conducted two successful sounding rocket experiments in conjunction with the Naval Research Laboratory (NRL) and are funded for a third experiment in early 1994. The NPS portion of these experiments has been passive sensing of the middle ultraviolet region of the electromagnetic spectrum by the Middle Ultraviolet Spectrograph (MUSTANG) instrument.

The evolution of this research has brought forth a desire to examine the Far and Extreme Ultraviolet regions of the electromagnetic spectrum (FUV and EUV, respectively) at moderate to high resolution. Moderate resolution instruments allow the study of

atmosphere dynamics through the examination of the Doppler shifts of emission lines. High resolution instruments have the capability to measure emission line profiles and thus permit the investigation of radiation transport through the examination of optically thick lines. (Cleary, et al., 1992)

## **A. THESIS OBJECTIVES**

The main objective of this thesis project was to validate the design of a high resolution All-reflection Michelson Interferometer for use in the FUV region of the electromagnetic spectrum. This validation was to be accomplished through the use of computer ray tracing procedures and fourier analysis. A secondary objective was to further examine and optimize various parameters of the instrument in order to propose design revisions. The interferometer design was originally examined in detail by Wallace (1992) and Professor David D. Cleary of the NPS Physics department. This research is a continuation of those efforts.

## **B. THESIS OUTLINE**

Chapter II of this thesis provides background information regarding the composition of the atmosphere. The importance of atmospheric research and the significance of this project in the area of high resolution spectroscopy are also discussed. The third chapter gives a basic review of the theory of interference and diffraction and an introduction to the All-reflection Michelson Interferometer (AMI). The simulation of the Oxygen 1304 Å triplet emission line profile is then presented. Chapter IV introduces the ray tracing software used and discusses its limitations. The fifth chapter explains the procedure used in conducting this research and presents the specific results obtained. Finally, Chapter VI offers conclusions and makes recommendations for further study in this area. Two appendices are included which contain ray tracing parameter files and program listings.



## II. BACKGROUND

### A. ATMOSPHERIC COMPOSITION

The Earth's atmosphere is generally divided into regions based on kinetic temperature or on chemical composition. The four main temperature regions or "spheres" of the earth have characteristic temperature gradients and are separated by nearly isothermal transition regions referred to as "pauses". The lowest temperature shell is the troposphere, the area of the atmosphere where surface weather exists. The troposphere has a negative temperature gradient and extends from the Earth's surface to an altitude of approximately ten kilometers. It is followed at an altitude of 10-12 km by the tropopause. The second region, extending from approximately 12 km to 50 km in altitude, is the stratosphere. The stratosphere maintains a positive temperature gradient mainly due to heating caused by the ozone layer (discussed below). It is followed by the stratopause. Above the stratopause is the mesosphere, characterized by a negative temperature gradient. Above the mesosphere is the mesopause, followed by the thermosphere and thermopause. The thermosphere is heated primarily by the absorption of electromagnetic radiation by molecular oxygen in the range of 1000 Å to 2000 Å. This warming initiates a final temperature gradient reversal. In the thermosphere, interaction between solar radiation and atmospheric gases forms the region of ionized particles known as the ionosphere. The temperature regimes and the associated kinetic temperature profile are shown in Figure 1. (Tascione, 1988)

The Earth's chemical composition spheres, also shown in Figure 1, begin with the homosphere. This region extends from the Earth's surface to an altitude of approximately 100 km. In the homosphere, eddy diffusion or convective atmospheric mixing, keeps the relative concentrations of component gasses effectively constant. Within the homosphere lies the ozone layer at an altitude of about 30 km. The ozone layer absorbs nearly 100% of solar UV radiation between approximately 2000 Å and 2900 Å. It is subsequently the

main cause of atmospheric warming in the stratosphere. Above the homosphere, beginning at approximately 80-100 km, is the heterosphere. Here, the rate of convective mixing drops off exponentially with altitude. The primary transport mechanism in this region is therefore molecular diffusion. As a result, the constituent species diffuse through the region to maintain hydrostatic equilibrium. Finally, the exosphere extends from approximately 500 km to 1000 km and above. In the exosphere, high energy neutral particles tend to escape the Earth's atmosphere due to their high kinetic energies and the infrequency of collisions in this region. The low collision frequency is a consequence of the low density of atmospheric particles and therefore the large mean free path. (Tascione, 1988)

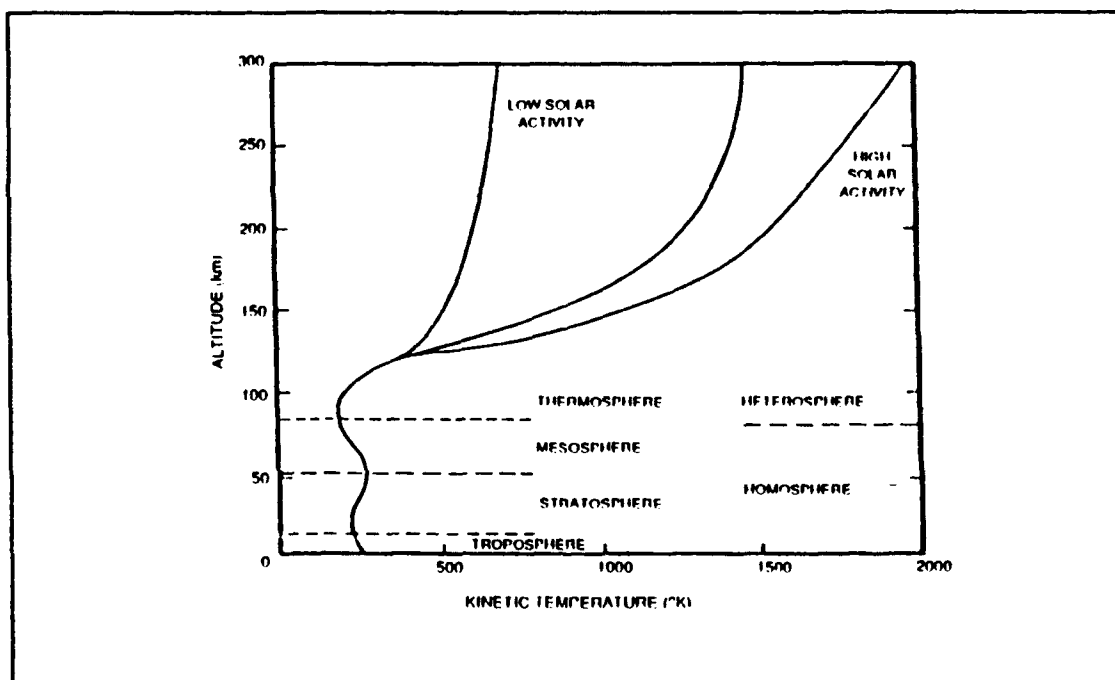


Figure 1 Temperature and Composition Spheres of the Atmosphere (from Tascione, 1988)

## **B. MOTIVATION FOR STUDY**

### **1. Naval Postgraduate School Research**

As discussed above, NPS has conducted two sounding rocket experiments. These experiments were made from the White Sands Missile Range in New Mexico using the MUSTANG instrument. They were made in conjunction with the Naval Research Lab's High Resolution Airglow and Aurora Spectrograph (HIRAAS). MUSTANG uses an Ebert-Fastie spectrograph to examine a band from 1800 to 3400 Å, primarily measuring emissions from N<sub>2</sub> and NO with a resolution of approximately 10 Å. The follow-on version of the MUSTANG instrument is the higher resolution Ionospheric Spectroscopy and Atmospheric Composition (ISAAC) instrument, scheduled for launch in 1995 aboard a low earth orbit satellite.

### **2. Motivation for High Resolution Spectroscopy**

The 10 Å resolution of the MUSTANG instrument will be greatly improved by ISAAC with a resolution of 1.5 Å; however, there is still a need for new instruments with even greater resolution. The All-reflection Michelson Interferometer (AMI) is such an instrument. With an expected resolution on the order of a few mÅ, this instrument will enable atmospheric researchers not only to obtain more accurate kinetic temperature data but also to more closely study emission line profiles. In depth study of emission line profiles will facilitate a better understanding of the physics of the underlying radiative transport mechanisms (Cleary, et al., 1992). The specific motivation behind the version of the All-reflection Michelson Interferometer presented herein is the requirement to measure the altitude distribution of atomic oxygen. The AMI instrument will permit the direct measurement of the triplet profile at 1304 Å. From this measurement, the density of atomic oxygen in the thermosphere can be calculated without the requirement for complex chemical models or absolute instrument sensitivity (Cleary, et al., 1993). Moreover, the design

discussed here can be adapted to examine line profiles of numerous atmospheric species, providing a better understanding of the make-up of the ionosphere. This area of study is of particular interest to the DoD owing to the importance of the ionosphere in the range prediction and propagation characteristics of over-the-horizon RADAR and long-range radio communications.

### III. THEORY

This section introduces the basic theory required to understand the method, results, discussion and conclusions regarding the All-reflection Michelson Interferometer. A short description of the mathematical function used to model the line profile of interest is first presented. A general overview of interference and diffraction theory is then given followed by a description of the All-reflection Michelson Interferometer.

#### A. SOLAR OXYGEN 1304 Å TRIPLET LINE PROFILE

In order to study the characteristics of the AMI with respect to the 1304 Å triplet, a simple but accurate model of that profile was required. A straightforward model developed in detail by Gladstone (1992) was chosen. This model uses the sum of two equal and offset gaussians to model the self-reversed spectral line profile according to the equation

$$\pi F(x) = \left[ \frac{\pi F}{2\sqrt{\pi}x_{\text{dis}}} \right] \left[ e^{-\left(\frac{x-x_{\text{off}}}{x_{\text{dis}}}\right)^2} + e^{-\left(\frac{x+x_{\text{off}}}{x_{\text{dis}}}\right)^2} \right], \quad (1)$$

where  $\pi F(x)$  is the flux in  $\text{ergs cm}^{-2} \text{sec}^{-1} (\text{km/sec})^{-1}$ ,  $x$  is the Doppler velocity in  $\text{km/sec}$  (converted to wavelength below), and  $\pi F$  is the line integrated flux in  $\text{ergs cm}^{-2} \text{sec}^{-1}$ . The quantities  $x_{\text{off}}$  and  $x_{\text{dis}}$  are Doppler velocities and are described by Gladstone as a measure of the offset of the emission peaks from the center of the self-reversed line and a measure of the dispersion of the line, respectively.

For the purposes of this thesis,  $x_{\text{off}}$  and  $x_{\text{dis}}$  were converted from Doppler velocity (in km/sec) to Doppler wavelength shift,  $\Delta\lambda$  (in meters), in the following fashion. First, the Doppler wavelength shift is defined by,

$$\Delta\lambda = \frac{\lambda_0 x}{c}, \quad (2)$$

where  $x$  is a Doppler velocity as in Equation (1) and  $c$  is the velocity of light.  $\lambda_0$  is the center wavelength and  $\lambda = \lambda_0 + \Delta\lambda$ . Therefore,

$$x = \frac{c\Delta\lambda}{\lambda_0}. \quad (3)$$

Substituting  $\Delta\lambda = \lambda - \lambda_0$ , gives

$$x = \frac{c(\lambda - \lambda_0)}{\lambda_0} = \frac{c\lambda}{\lambda_0} - c, \quad (4)$$

therefore, the equations for the offset and dispersion with respect to wavelength become,

$$x_{\text{off}} = \frac{\lambda_{\text{off}} c}{\lambda_0} - c \quad (5)$$

$$x_{\text{dis}} = \frac{\lambda_{\text{dis}} c}{\lambda_0} - c. \quad (6)$$

Substituting the above two equations into Equation (1) gives

$$\pi F(\lambda) = \frac{\pi F}{2\sqrt{\pi}\left(\frac{c\lambda_{\text{dis}}}{\lambda_0} - c\right)} \left[ e^{-\frac{(\lambda - \lambda_{\text{off}})^2}{(\lambda_{\text{dis}} - \lambda_0)^2}} + e^{-\frac{(\lambda - 2\lambda_0 + \lambda_{\text{off}})^2}{(\lambda_{\text{dis}} - \lambda_0)^2}} \right] \quad (7)$$

Equation (7), giving flux as a function of wavelength, is determined by the parameters  $\lambda_{\text{off}}$  and  $\lambda_{\text{dis}}$ , given by rearranging Equations (5) and (6) to get

$$\lambda_{\text{off}} = \lambda_0 \left( \frac{x_{\text{off}}}{c} + 1 \right) \quad (8)$$

$$\lambda_{\text{dis}} = \lambda_0 \left( \frac{x_{\text{dis}}}{c} + 1 \right). \quad (9)$$

Equations (7), (8) and (9) were used to model the emission line profile in the IDL programming language as discussed in Chapter V.

## B. INTERFERENCE AND DIFFRACTION

Basic to an understanding of the background, procedures and results of this thesis is a general understanding of the concepts of interference and diffraction and their applicability in the area of spectroscopy. Interference and diffraction theory are presented separately below. More complete coverage of these two subjects is available in any number of standard texts on basic physics, electromagnetic theory, or optics such as Pedrotti and Pedrotti (1987).

## 1. Interference Theory

Interference can be described as the enhancement or diminution of the intensity of electromagnetic radiation caused by the superposition of two or more individual waves. The classical interference of two waves causes alternate enhancement and reduction of wave intensity in what can be described as an interference or fringe pattern.

In classical two beam interference, two electromagnetic waves, represented by their vector components  $E_1$  and  $E_2$ , emanate from a single source, travel along different paths and then recombine at some point P identified by its position vector  $r$ . Assuming that the waves are of equal amplitude, they can be described by

$$E_1 = E_0 \cos(k_1 \cdot r - \omega t) \quad (10)$$

$$E_2 = E_0 \cos(k_2 \cdot r - \omega t + \phi), \quad (11)$$

where  $E_0$  represents the amplitude;  $\phi$ , the initial phase difference;  $\omega$ , the wave frequency; and  $k$ , the propagation vector. At the point of recombination, P, the electromagnetic field is given by the superposition of  $E_1$  and  $E_2$ ,

$$E_P = E_1 + E_2. \quad (12)$$

In optics, electromagnetic waves are more conveniently represented by their irradiance  $I$ , the value that is commonly measured. Irradiance is related to the electric field vector by  $I = \epsilon_0 c \langle E^2 \rangle$ , with  $\epsilon_0$  the permittivity constant,  $c$  the speed of propagation, and the angled brackets indicating the time average of the quantity inside. At point P the irradiance is,

$$I_P = \epsilon_0 c \langle E_P^2 \rangle = \epsilon_0 c \langle E_1^2 + E_2^2 + 2E_1 \cdot E_2 \rangle, \quad (13)$$



or,

$$I_p = I_1 + I_2 + I_{12}, \quad (14)$$

where  $I_1$  and  $I_2$  are the irradiances of the constituent waves and  $I_{12}$  is an additional irradiance term due to the interference. This interference term is then

$$I_{12} = 2 \epsilon_0 c \langle \mathbf{E}_1 \cdot \mathbf{E}_2 \rangle. \quad (15)$$

Through the use of trigonometric identities and the time average characteristics of the trigonometric functions below,

$$\langle \sin^2(\omega t) \rangle = 1/2 \quad (16)$$

$$\langle \cos^2(\omega t) \rangle = 1/2 \quad (17)$$

$$\langle \sin(\omega t) \cos(\omega t) \rangle = 0, \quad (18)$$

the time average term of the interference becomes

$$\langle \mathbf{E}_1 \cdot \mathbf{E}_2 \rangle = 1/2 E_0^2 \cos[(\mathbf{k}_1 - \mathbf{k}_2) \cdot \mathbf{r} + \phi], \quad (19)$$

where the term in square brackets represents the phase difference between the constituent waves, hereafter denoted by  $\delta$ . The interference term of the irradiance is then

$$I_{12} = \epsilon_0 c E_0^2 \cos \delta. \quad (20)$$

Using the time average characteristic of  $\cos^2(\omega t)$  above, the irradiance terms representing the original two waves become

$$I_1 = I_2 = \frac{\epsilon_0 c E_0^2}{2} = I. \quad (21)$$

Therefore the interference term becomes,

$$I_{12} = 2 I \cos \delta \quad (22)$$

and the irradiance at point P is then

$$I_p = 2 I + 2 I \cos \delta. \quad (23)$$

The irradiance therefore becomes a maximum when  $\cos \delta$  is +1 or  $\delta = 2m\pi$ , ( $m = 0, \pm 1, \pm 2, \dots$ ) and a minimum when  $\cos \delta$  is -1 or  $\delta = (2m+1)\pi$ , ( $m = 0, \pm 1, \pm 2, \dots$ ). (Pedrotti and Pedrotti, 1987)

As described above, two beam interference is the periodic enhancement and reduction of the irradiance of two superimposed waves. It is caused by the phase shift,  $\delta$ , between the waves and can occur when the planes of constant phase (or wavefronts) are split among different paths. The total phase shift,  $\delta$ , is due to the combination of the initial phase shift of the waves and the difference in path length between the two beams. Two beam interference theory can be generalized to describe wavefront division interference of multiple waves.

A final important aspect of interference is the concept of coherence length. Optical waves do not travel in perfect and infinite sinusoids. They travel in groups that appear sinusoidal for a finite length and then discontinuously change phase as the next group begins. The average lifetime of the group is called the coherence time; the average length of this coherent pulse is referred to as the coherence length and varies with the source of electromagnetic energy (Pedrotti and Pedrotti, 1987). Its importance lies in the fact that for interference to take place, paired groups of waves must arrive together at the field point, P. If the path length difference is greater than the coherence length, paired groups do not arrive within the coherence time, and interference does not occur. Throughout the con-

duct of this thesis, coherence length was arbitrarily and artificially set to a very high value such that it was effectively infinite.

## 2. Diffraction Theory

Diffraction is similarly an effect of the wave nature of light. Diffraction is described by Pedrotti and Pedrotti (1987) as "...any deviation from geometrical optics that results from the obstruction of a wavefront of light." Interference between diffracted waves produces a pattern of fringes. As shown in Figure 2 below, the diffraction of light by multiple slits produces a fringe pattern consisting of bright, distinct and widely separated maxima. A diffraction grating is a device containing evenly spaced, multiple slits or grooves that takes advantage of the sensitivity of its diffraction pattern to the wavelength of the incident light.

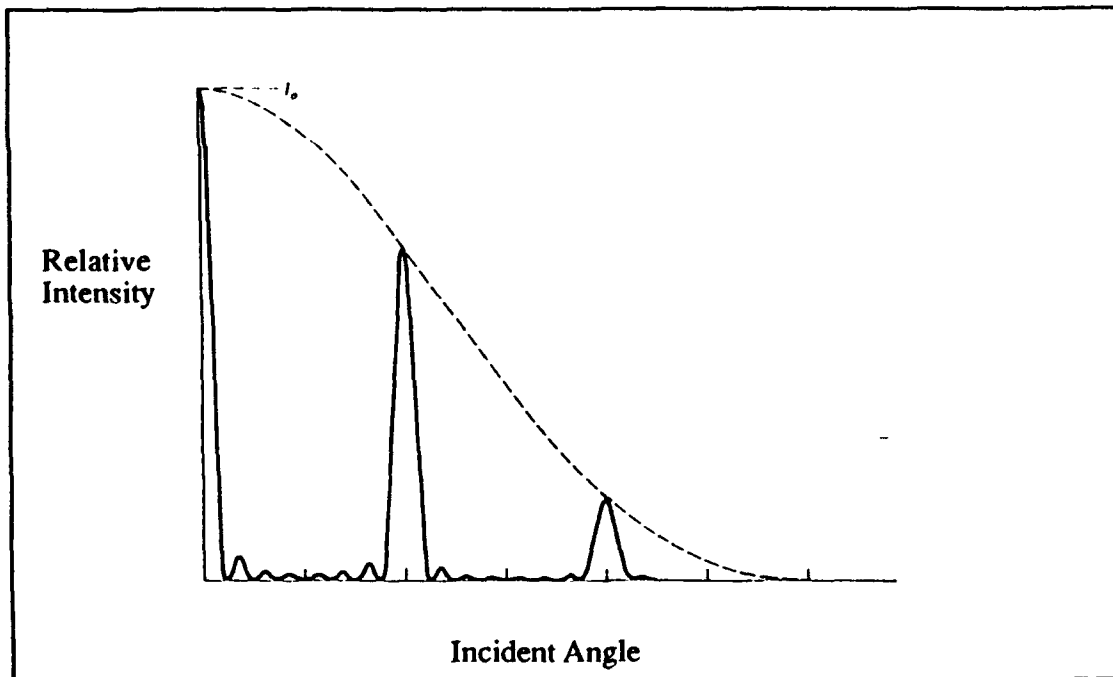


Figure 2 Pattern for Multiple Slit Fraunhofer Diffraction (Pedrotti and Pedrotti, 1987)

Far field or Fraunhofer diffraction is diffraction where the observation plane is a large distance from the diffraction source such that the wavefronts can be considered pla-

nar. In classic Fraunhofer diffraction, multiple slit diffraction using a grating produces irradiance maxima (as shown in Figure 2 above) according to the grating equation

$$m\lambda = a (\sin\theta_i + \sin\theta_m) . \quad (24)$$

Here  $m$  is the order of diffraction,  $\theta_i$  and  $\theta_m$  are the incident and diffraction angles measured from the grating normal, and  $a$  is the distance between slits on the grating. Usually the grating ruling density,  $\rho = 1/a$ , is given and the grating equation then becomes

$$\rho m\lambda = (\sin\theta_i + \sin\theta_m) . \quad (25)$$

Therefore, a diffraction grating takes a beam of monochromatic incident light and, upon reflection from the grating, splits it along multiple paths according to the grating equation. The zero order diffraction path is the same for all wavelengths and is merely a reflection following Snell's law. Positive order diffractions diffract light at an angle greater than that of the zero order and negative order diffractions diffract light at an angle less than that of the zero order. As can be seen in Figure 2 above, the intensity of the diffracted beam falls off as the diffraction angle (and thus diffraction order) increases in absolute value.

Figure 3 shows an illustration of a diffraction grating with multiple orders of diffraction.

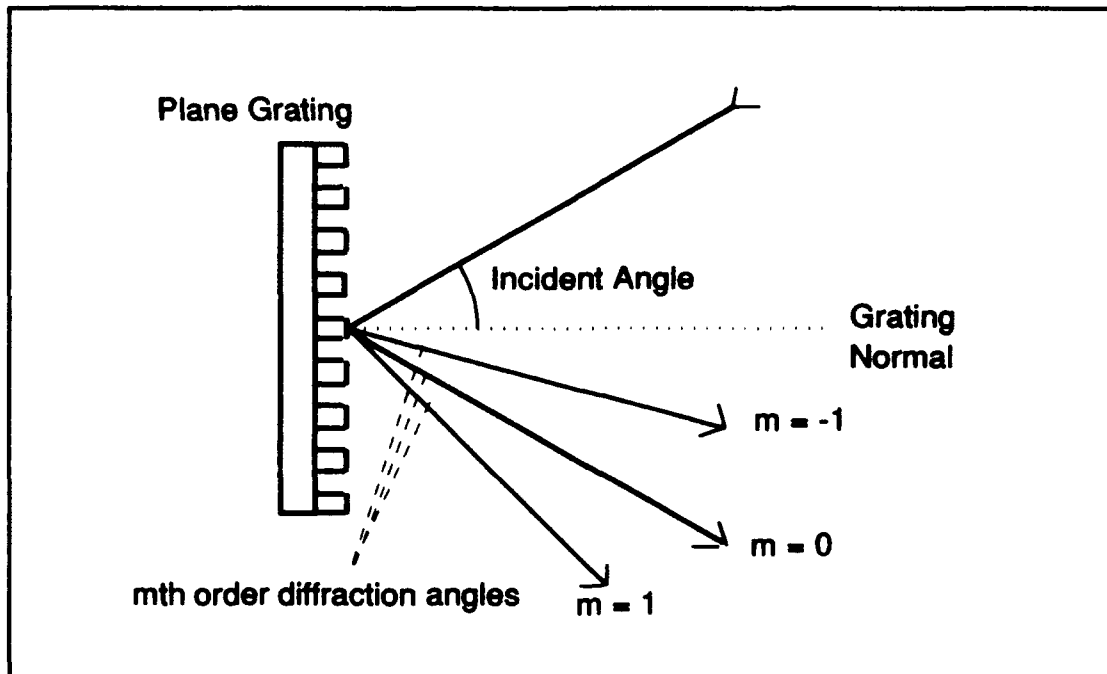


Figure 3 Reflection Grating with Multiple Diffraction Orders

There is no fundamental physical difference between interference and diffraction patterns. Fringes caused by the diffraction of light are more rigorously termed interference fringes, but are commonly called diffraction patterns. The words interference and diffraction are often used interchangeably; however, in this thesis, interference will refer to the effect producing a fringe pattern while diffraction will refer to the change in direction of a beam caused by an obstruction or aperture.

### C. THE ALL-REFLECTION MICHELSON INTERFEROMETER

An interferometer is a device that splits and then recombines light to create a pattern of interference fringes for a specific purpose. Generally classified by the method used to separate the incident beam of light, interferometers are termed either amplitude or wave-front splitting devices. This section discusses the basic theory behind the plane grating All-reflection Michelson Interferometer. The AMI is classed as an amplitude splitting

device because of the use of a diffraction grating as a beam splitter to divide the input beam among separate paths.

The general design for the All-reflection Michelson Interferometer examined in this thesis was developed in detail by Wallace (1992). This basic all-reflection interferometer design consists of an aperture, a plane diffraction grating, two plane mirrors, and a detector. The grating splits the input light into two paths corresponding to the zero- and minus-one-order diffraction. Each path travels to a plane mirror which reflects the light back to the grating. The light again reflects off the grating utilizing the minus-one and zero diffraction orders, respectively. The light finally recombines along a common path from the grating to the detector. The input light is assumed to be monochromatic and collimated for the purposes of this discussion. The general layout of the elements of the All-reflection Michelson Interferometer is shown in Figure 4. Figure 5 shows the path of several rays in the AMI.

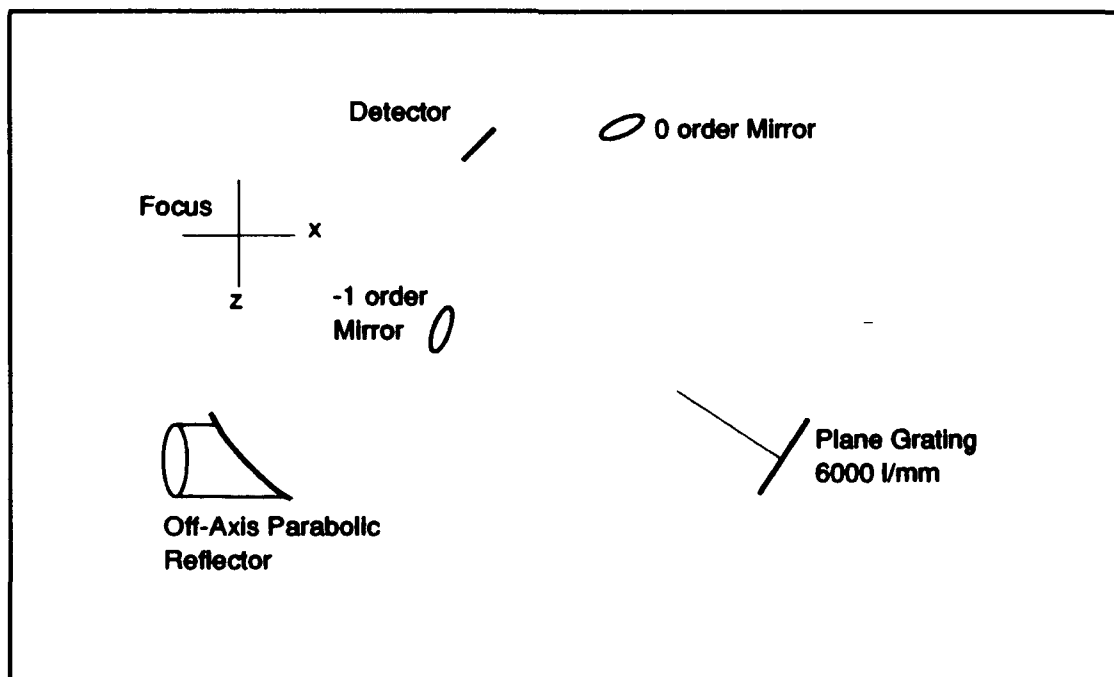


Figure 4 Typical All-reflection Michelson Interferometer Setup

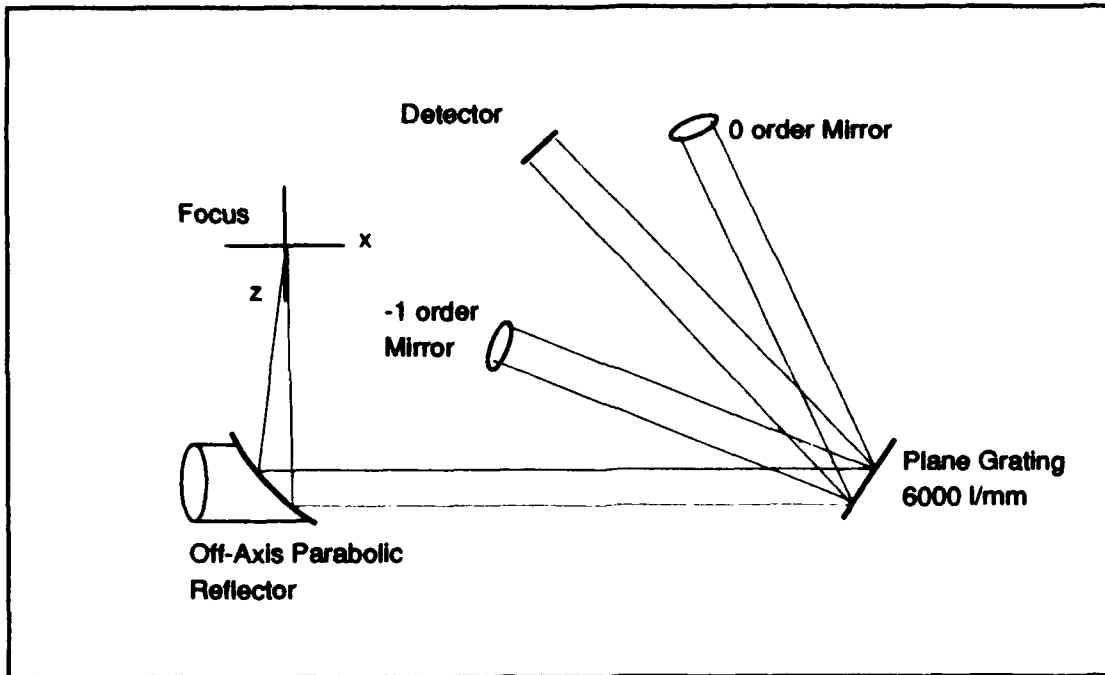


Figure 5 Ray Paths in a Typical All-reflection Michelson Interferometer.

In the AMI, the path length measured along each of the two paths (henceforth known as the “zero-order path” and the “minus-one-order path”) is equal. When the wavelength of the input light is equal to the “tuned” wavelength (known as  $\lambda_0$ ), the wavefronts of the two recombined beams are parallel. The interference at the detector is constructive at all points and the interference pattern has zero spatial frequency. When the wavelength of the incident light is offset from  $\lambda_0$ , however, a shift in the diffraction angles from that of the tuned wavelength results. This shift causes a tilt between the wavefronts of the two beams. The spatial frequency of the resulting interference pattern is wavelength dependent. The fourier transform of this spatial fringe pattern indicates the amount of wavelength offset,  $\Delta\lambda$ , from the tuned wavelength, where  $\Delta\lambda = \lambda - \lambda_0$ . The instrument presented here, however, is incapable of differentiating between equal offsets both greater and less than  $\lambda_0$ . A more detailed treatment of the so-called spatial heterodyning effect can be found in Wallace (1992).

Recall that the AMI is designed so that the length of each of the two paths is equal. The angles of incidence and diffraction, and the placement of the mirrors are determined as described below. In the AMI design, use of a plane diffraction grating serves to diffract the incident light along paths according to the general grating equation (Equation (25)), repeated here,

$$\rho m \lambda = \sin \theta_i + \sin \theta_m, \quad (26)$$

where again  $\rho$  is the grating density (lines /mm),  $m$  is the diffraction order,  $\lambda$  is the wavelength (mm), and  $\theta_i$  and  $\theta_m$  are the incident angle and the  $m^{\text{th}}$  order diffraction angle, respectively. All angles are measured clockwise from the grating normal. In order that the zero- and minus-one-order paths have equal lengths, their respective mirrors must be equidistant from the grating.

Multiple diffraction orders emanating from the grating reduce the overall intensity of light incident upon the detector. As the instrument only uses the zero- and minus-one-order initial diffractions, the light incident upon the detector can be maximized by eliminating all diffractions of higher order. This is done by proper selection of  $\rho$  with respect to  $\lambda$  so that  $\theta_1$  and all higher order diffraction angles are greater than or equal to  $90^\circ$  and  $\theta_{-2}$  and all lower order diffraction angles are less than or equal to  $-90^\circ$  (Cleary, et al., 1992).

Setting  $\theta_1$  equal to  $90^\circ$  and substituting into Equation (26) above gives,

$$\rho \lambda = \sin \theta_i + 1 \quad (27)$$

or,

$$\theta_i = \text{asin}(\rho \lambda - 1). \quad (28)$$



Similarly, setting  $\theta_2$  to  $-90^\circ$  and substituting into the grating equation gives

$$-2\rho\lambda = \sin\theta_i - 1 \quad (29)$$

or,

$$\theta_i = \text{asin}(-2\rho\lambda + 1) . \quad (30)$$

Substituting Equation (28) into Equation (30) and solving for  $\rho$  gives

$$\rho = \frac{2}{3\lambda} . \quad (31)$$

Equation (31) gives the optimum ruling density with respect to wavelength for minimum loss of light intensity due to wasted diffraction orders. In practice, one selects the closest commercially available grating with a grating density greater than or equal to that given in Equation (31) above. (Wallace, 1992)

In fact, as pointed out by Wallace (1992), selection of a grating density precisely equal to that given above would force the incident and minus-first-order diffraction angles to be identical, an undesirable characteristic for this application as the minus-one-order mirror would then be in the path between the grating and source. Therefore, Equation (31) has been established by Wallace (1993) as the minimum acceptable grating density for the elimination of wasted orders at the first pair of diffractions. Once selection of the grating density, wavelength of interest, and incident angle has been completed, the positions of the components of the interferometer are determined by the grating equation. For the zero order mirror,

$$\theta_0 = -\theta_i \quad (32)$$

and for the minus first order mirror,

$$\theta_{-1} = \text{asin}(-\rho\lambda - \sin\theta_i). \quad (33)$$

The final position of each of the components can be made after choosing the distances from the grating to the source, mirrors, and detector. This selection can be based almost entirely on size constraints of the completed instrument. Selection of the angle of incidence will be treated in Chapter V of this thesis.

## IV. RAY TRACING PROCEDURES

The method of ray tracing was used to model interference patterns for several versions of the proposed instrument. Additionally, once the instrument layout was finalized, numerous interference simulations were performed to determine some final performance parameters of the instrument. This chapter contains a short description of the software used for ray tracing and interference pattern construction and describes limitations of the software for the present application.

### A. DART RAY TRACING PROGRAM

The majority of the results presented in this thesis were developed by simulating the instrument using the DART ray tracing program of Atkinson (1993). DART is a Windows-based PASCAL program written for the IBM PC. It was specifically designed for complex optical ray tracing applications and is described in detail by Atkinson (1993). In DART, instruments are modeled by combining components from an extensive element library. Apertures in the DART program (hereafter called DART apertures) are modeled using a multi-function user interface and can be tailored in both shape and size to the specific application. The light source can be monochromatic radiation of any wavelength or can be composed of multiple wavelengths at selectable intensities.

DART uses two three-dimensional right-hand coordinate systems for the placement of optical elements. The first, called the "global" coordinate system is used for the placement of instrument elements in relation to the instrument aperture which is usually at the origin. The initial direction of the input beam is in the positive Z direction. The most common layout of a planar instrument is to place all elements in the X-Z plane. The second coordinate system is the "local" coordinate system. This set of coordinates is fixed with

respect to each element in the system. The origin of each local coordinate system is centered on the element with the z-axis in the direction of the outward normal of the element surface. Translation and rotation of an element changes its position and direction in the global coordinate system but not in the local system. Throughout this thesis, axes and directions described by capital letters will denote global coordinates while lower case letters will indicate the local coordinates. An illustrative two-element instrument with the coordinate systems indicated is shown in Figure 6.

The DART program produces a rough layout of the instrument being modeled which can be viewed from any angle. If desired, DART traces the ray paths on this layout display. DART layout drawings only trace those rays that contact the next element in sequence—missed rays are not drawn. Plane surfaces may be used to mask off undesired rays anywhere in the instrument. The final plane surface in any instrument serves as the instrument's detector. The specific layout for the AMI is described in detail in Chapter V.

The interference patterns, or interferograms, produced by DART are viewed in an interference "window" on the computer screen. An interference profile, created by vertically summing the 400 element wide interferogram, may be saved as a binary data file. The result is a file consisting of 400 pairs of intensity-versus-detector-x-position values. Additionally, an instrument parameter file may be created which contains a complete listing of the input parameters for the selected instrument path.

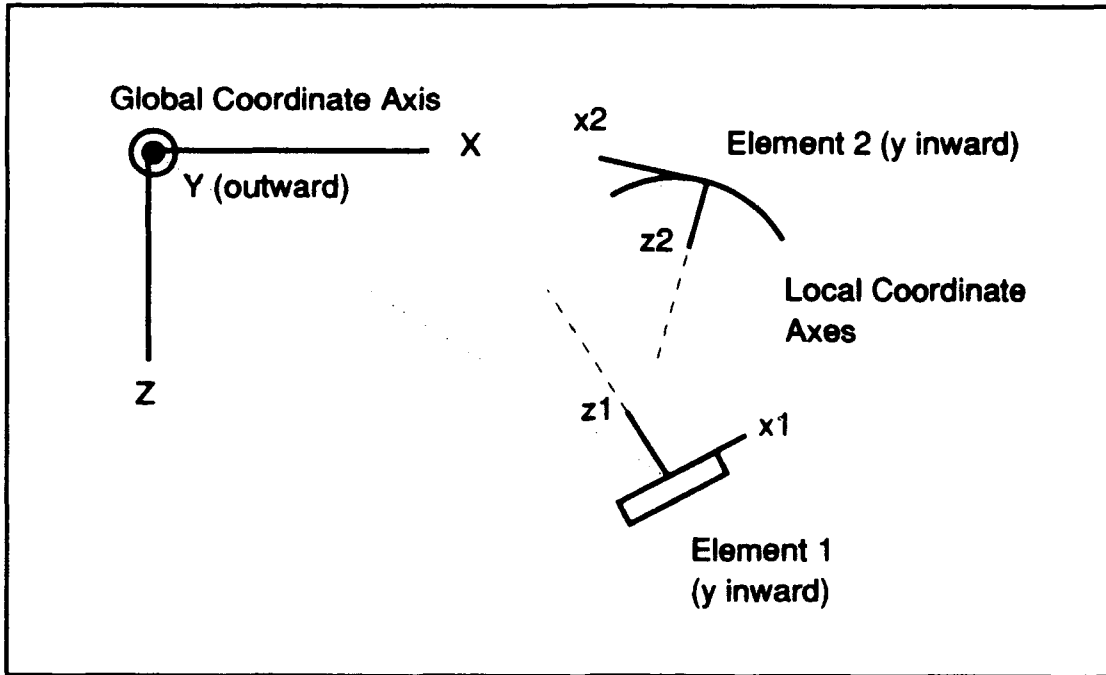


Figure 6 Global and Local Coordinate Systems

## B. RAY TRACING SOFTWARE LIMITATIONS

Although of inestimable benefit, the DART program contains several features which limit its usefulness in the present application. The first of these is the limit of 400 bins in which to sum the interference data. This 400 bin limit constrains the resolution demonstrable by DART interference files compared to a 512 or 1024 pixel one-dimensional array detector (two commonly available sizes). The number of bins in DART was based on the limit of screen resolution on a typical computer monitor. A suggested improvement is to include an option to select greater numbers of bins and have DART calculate ray paths and interference patterns at a higher resolution than can be displayed on the screen. As most of the analysis of ray tracing results will, in all likelihood, be done using other, more robust calculating programs such as IDL or FORTRAN, this change would be beneficial to most DART users.

A second limitation of the DART program is the requirement that the number of rays striking the detector be identical in the two instrument paths (for multiple wavelength interference). If the number of rays at each path's detector is unequal, interference is not calculated. Although not troublesome when using a small aperture and beam size combined with large components and a large detector, the limitation is often apparent when using small components. A more beneficial approach would have been for DART to discount rays from one path that can't be matched with rays from the other, while allowing the interference to be computed. DART could then alert the user to the number of unusable rays.

The final limitation of note is the requirement that rays emanating from the instrument aperture initially travel in the positive Z direction. This requirement can sometimes force the instrument designer to place a majority of critical components on the negative Z side of the X-axis. Although easily worked around, this complicates the translation from design on DART to placement of actual elements on an optical bench.

## V. EXPERIMENTAL PROCEDURE AND RESULTS

### A. IDL FOURIER TRANSFORM PROCEDURES

In the AMI, the spatial frequency of the interference pattern is wavelength dependent. One recovers the spectrum of the incident light source by taking the fourier transform of the interference profile. Interactive Data Language (IDL) for PC with Windows was used in order to examine the spectrum of the fringe patterns created by the DART application. An IDL procedure was written to read interference data from a DART output file and then take the fast fourier transform of that data using the IDL FFT function. The procedure plots the interference profile (relative intensity versus the  $x$ -axis position of the detector) and the fast fourier transform spectrum (relative intensity versus position in the FFT array). IDL places the fourier transformed data into an array of the same dimensions as the input data and then plots the full FFT spectrum consisting of both positive and negative (ghost) frequencies.

For the purposes of this thesis, the full FFT spectrum contains redundant information. A so-called wavelength spectrum was obtained by taking one half of the full FFT spectrum and converting the horizontal axis to wavelength. For clarity of presentation, positive frequencies of the fourier transform were used for incident wavelengths greater than  $\lambda_0$  and negative frequencies for wavelengths less than  $\lambda_0$ . In the present case, the fourier spectrum consists of 400 elements, half of which are used to plot the wavelength spectrum. FFT spectra were converted to wavelength spectra by another IDL procedure. These IDL plotting procedures and functions are also presented in Appendix A.

## B. EXPERIMENT DOCUMENTATION

The research conducted as part of this thesis produced three distinct forms of output. The DART interferogram is a two-dimensional representation of the interference pattern at the instrument detector. Each ray striking the detector is plotted using a gray scale based on the intensity of the interfering light. The interferogram is a representation of how interference would appear were the light source visible. The second form of output is the interference profile. This is a plot of intensity versus x-axis position; it represents the pattern that would be obtained from a one-dimensional array detector. The final and most useful form of output is the wavelength spectrum (or alternatively the full FFT spectrum). Once this plot is calibrated for wavelength, the peaks directly translate to the difference,  $\Delta\lambda$ , between input wavelength and tuned wavelength.

The quality of each of the plots listed above can be enhanced simply by increasing the number of rays produced at the DART aperture. However, speed of computation within DART is inversely related to the number of rays produced; therefore, most interference runs were completed using an intermediate number of rays. Documentation for this thesis was later prepared by re-running desired simulations using a greater number of rays.

In DART, intensities are relative values determined by the number of rays striking the detector. These intensities can be scaled by whole numbers when entering multiple wavelengths but absolute intensities are difficult to introduce. Additionally, intensities for line profiles calculated using Equation (7) have been scaled and rounded-off for ease of entry into DART. Since relative intensities are sufficient for this thesis, no attempt was made to introduce absolute intensities herein. Comparison of relative intensities, however, was used extensively in examining the behavior of the AMI.



### C. RAY TRACING PROGRAM SETUP

The setup of the AMI instrument in the ray tracing program was undertaken in three steps. First, the interferometer portion alone was modeled using a rectangular, collimated beam of monochromatic light as the source at the DART program aperture. Then an instrument aperture more closely resembling the planned AMI design was modeled using an off-axis parabolic reflector with the DART aperture at the focus of the paraboloid. Finally, these two DART applications were combined to form a model of the AMI. Additional elements are expected to be included in later models of the actual flight-qualified instrument in order to better collect and direct the light into the spectrograph aperture.

Once the complete instrument was modeled, several different versions of the DART aperture were created. DART's aperture determines the form of the light incident on the instrument's first element. The first version contained an ideal point source which consisted of rays emanating from a single point and spreading spherically from the DART aperture to the surface of the parabolic reflector. The second version used a circular "pin-hole" source ranging in diameter from 100  $\mu\text{m}$  to 500  $\mu\text{m}$ . The final version consisted of a vertical slit aperture of varying widths and a height of one centimeter. In both the pinhole and the slit, rays emanated and spread spherically outward from the entire surface area of the source. A more complete description of the three instrument setups is provided below.

#### 1. Interferometer

As described above, the interferometer section of the AMI instrument was modeled with the DART ray tracing application. The model consisted of a square aperture, a square diffraction grating, two plane circular mirrors, and a plane surface for use as a detector. The overall dimensions of the instrument were selected to be representative of those in a rocket or space-based version. The distances from the diffraction grating to the various elements are shown in Table I.

TABLE I. INTERFEROMETER DIMENSIONS

Element	Distance to Grating
Aperture	40 cm
Mirrors	20 cm
Detector	25 cm

The grating density of the instrument was then selected by using Equation (31) to determine the optimal minimum grating density. Substituting in the desired tuned wavelength of 1304 Å gives

$$\rho = \frac{2}{3\lambda} = \frac{2}{3(1.304 \times 10^{-4} \text{ mm})} = 5112 \frac{\text{lines}}{\text{mm}}, \quad (34)$$

which leads to a commonly available grating choice of  $\rho = 6000$  lines/mm. The initial size of each of the elements in the DART simulation was chosen to be large enough so that all light from the DART aperture would strike each element in turn and finally strike the detector. In that way, accuracy in placement and orientation of each element was less critical. The elements were placed and oriented according to the theory described earlier using the dimensions specified in Table I and the selected incident angle. Calculations and initial conversion into DART's coordinate system were simplified by using a MATHCAD document written by Wallace (1992). Once entered into the DART program, interference patterns were created by running DART's interference macro for a number of different wavelengths of monochromatic light. Recall that the DART program requires separate instrument layouts for each path. An isometric view of each path of the interferometer with one ray displayed is shown in Figure 7 and 8. The resulting interferogram for an

input wavelength of  $1304.02 \text{ \AA}$  is shown in Figure 9. All three figures were drawn by the DART program. Appendix B includes the DART parameter file for each path shown.

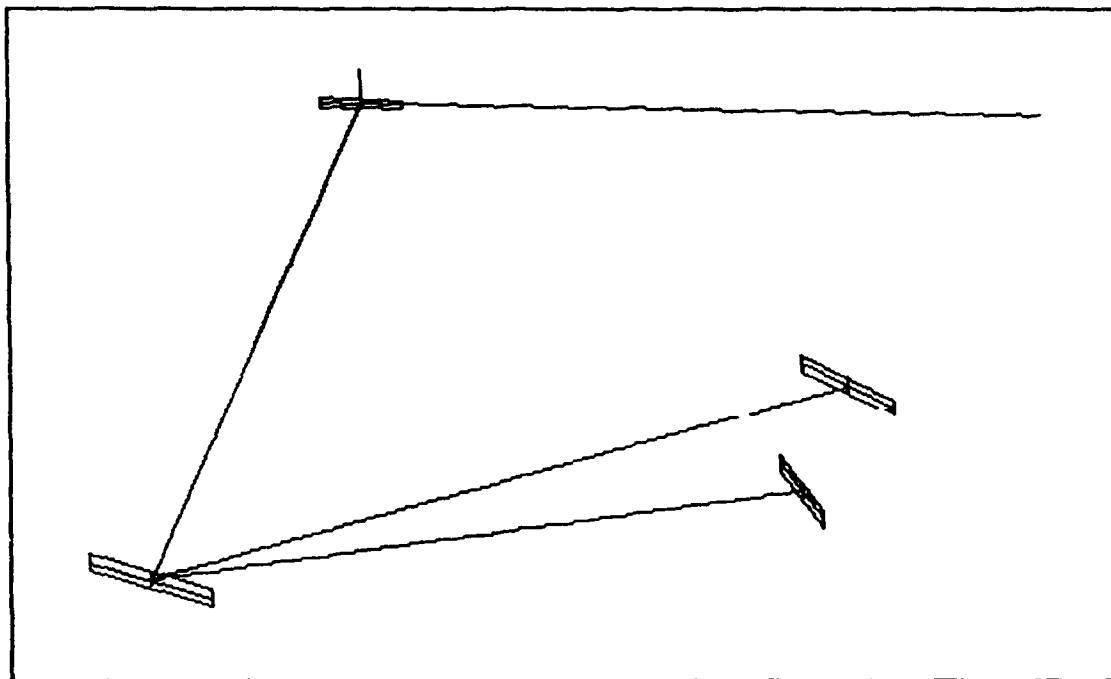


Figure 7 Interferometer Layout of the 0 Order Path Produced by DART (not to scale)

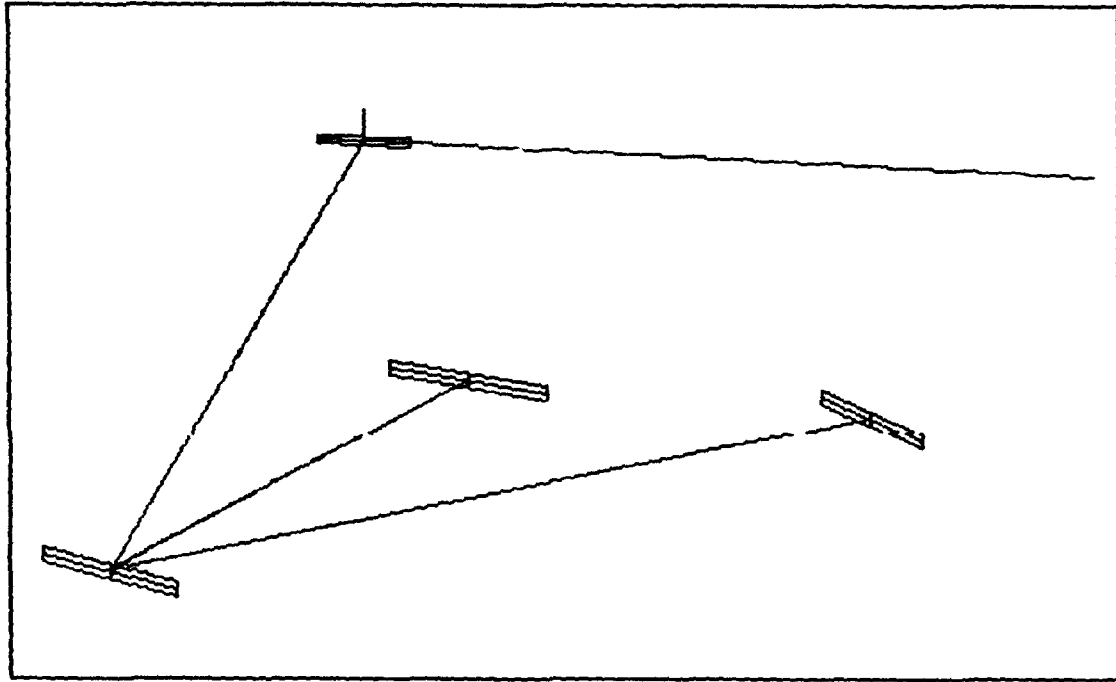


Figure 8 Interferometer Layout of the -1 Order Path Produced by DART (not to scale)

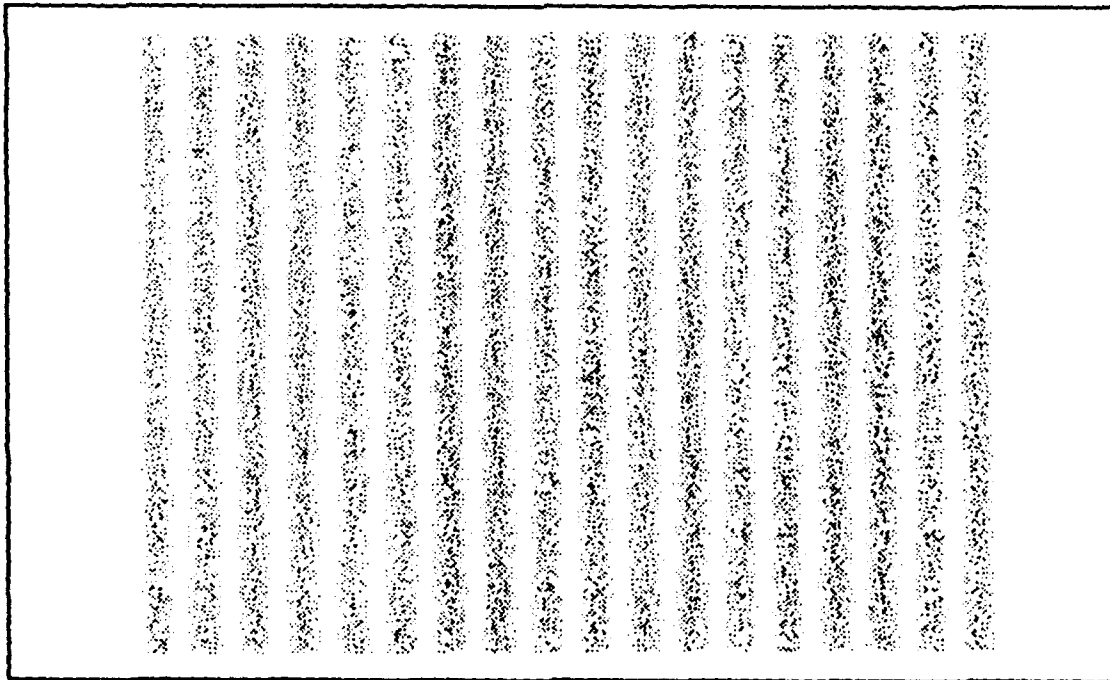


Figure 9 Interferogram for 1304.02 Å Incident Light (tuned to 1304.00 Å)

## 2. Off-axis Parabolic Reflector

The off-axis parabolic reflector was used as a collimating element between the source and the grating. The paraboloid was modeled in DART according to the specifications for the Oriel model 45347 parabolic reflector. This particular reflector was used by Risley (1993) in determining the physical problems associated with constructing the AMI for use in the visible and near ultraviolet spectrum.

In order to create an off-axis parabola in the DART application, the full parabolic mirror must first be entered. Then a plane surface mask must be placed between the parabola and the next element in sequence. The purpose of the mask, which is transparent to all rays striking it, is to eliminate all but those rays which would reflect off a real off-axis parabola. This is accomplished because DART only traces rays that strike the next element in sequence (see Chapter IV).

In order to accurately construct the DART version of the off-axis parabola, its orientation must be such that no rays are required in the negative Z direction of DART's global coordinate system (see Ray Tracing Software Limitations above). Therefore, the parabola was oriented as shown in Figure 10 below. This figure shows the general layout of the off-axis parabola and includes the trace of a small number of rays.

As can be seen in Figure 12 and in several of the interferograms, interference profiles and wavelength spectra that follow, the off-axis parabola introduces an increase in relative intensity of light on one side of the detector. This rise in intensity is due to a natural increase in the number of rays leaving the parabola mask on the side farthest away from the focus. Were the absolute intensity significant in this thesis, the rise would have to have been accounted for in subsequent analysis.

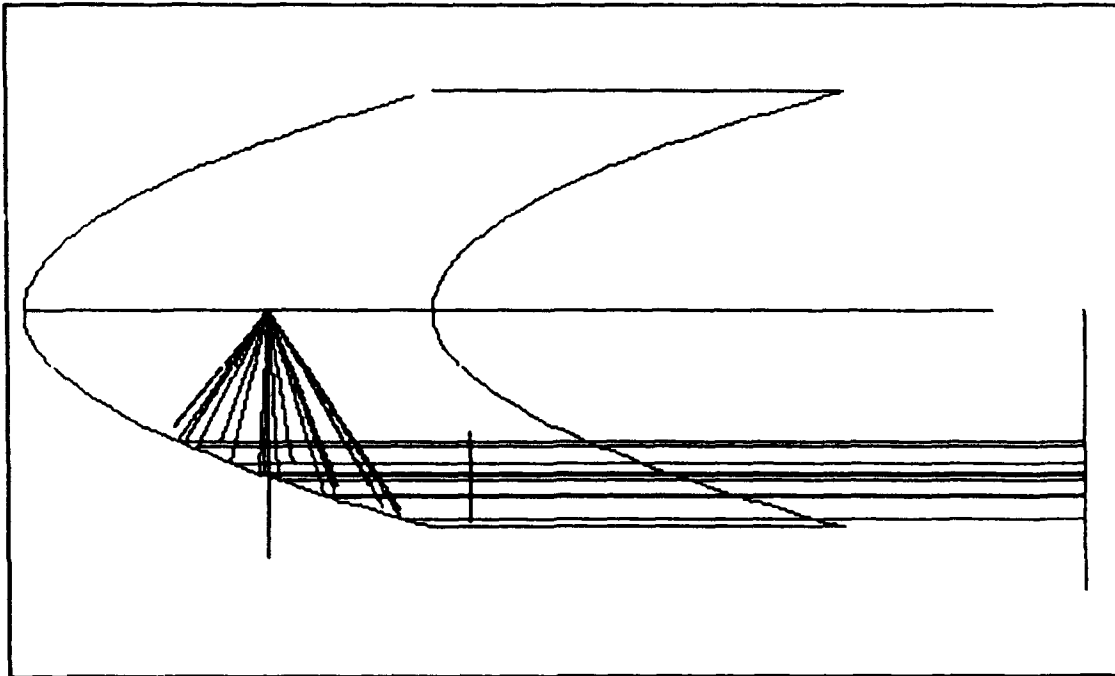


Figure 10 Off-axis Parabolic Reflector Simulation

### 3. All-Reflection Michelson Interferometer

The two sections of the instrument described above were combined into a single model forming the current version of the All-reflection Michelson Interferometer. This instrument was initially designed with all elements sized larger than required to ensure that all rays would strike the detector. After the model was rotated for the addition of the off-axis parabola, the interferometer section was placed 20 cm further from the DART aperture to facilitate adding additional optics to the simulation if required. The size of each element in the instrument was then reduced and the shape changed to more closely match commonly available components or components planned for use in other current NPS ionospheric research projects (Risley, 1993). The size and shape of the chosen components are shown in Table II.

TABLE II. COMPONENTS USED IN DART AMI SIMULATION

Component	Shape	Size (cm)
Grating	Square	5.0 x 5.0
Mirrors	Circular	d = 2.50
Detector	Rectangular	2.50 x 1.00

The complete instrument consists of two DART parameter files, each representing one path taken by the rays. These files are also included in Appendix B. The complete layout of the AMI used for all further DART interference runs is shown in Figures 11 and 12. Sample ray traces are also shown.

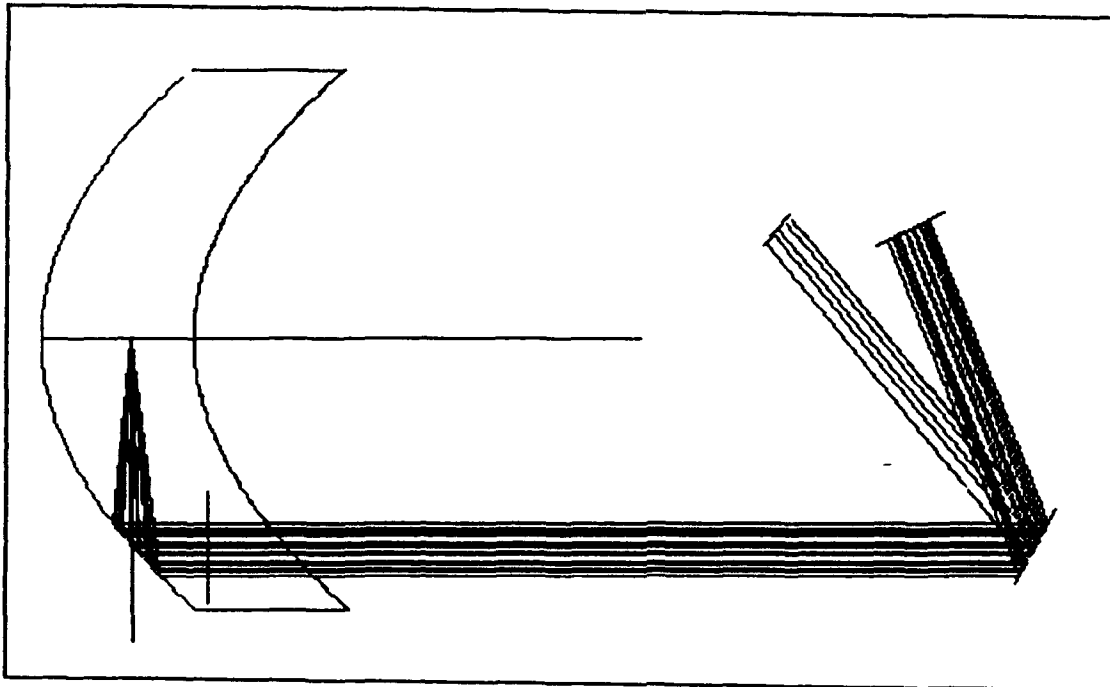


Figure 11 AMI DART Layout and Ray Trace of the Zero-Order Path

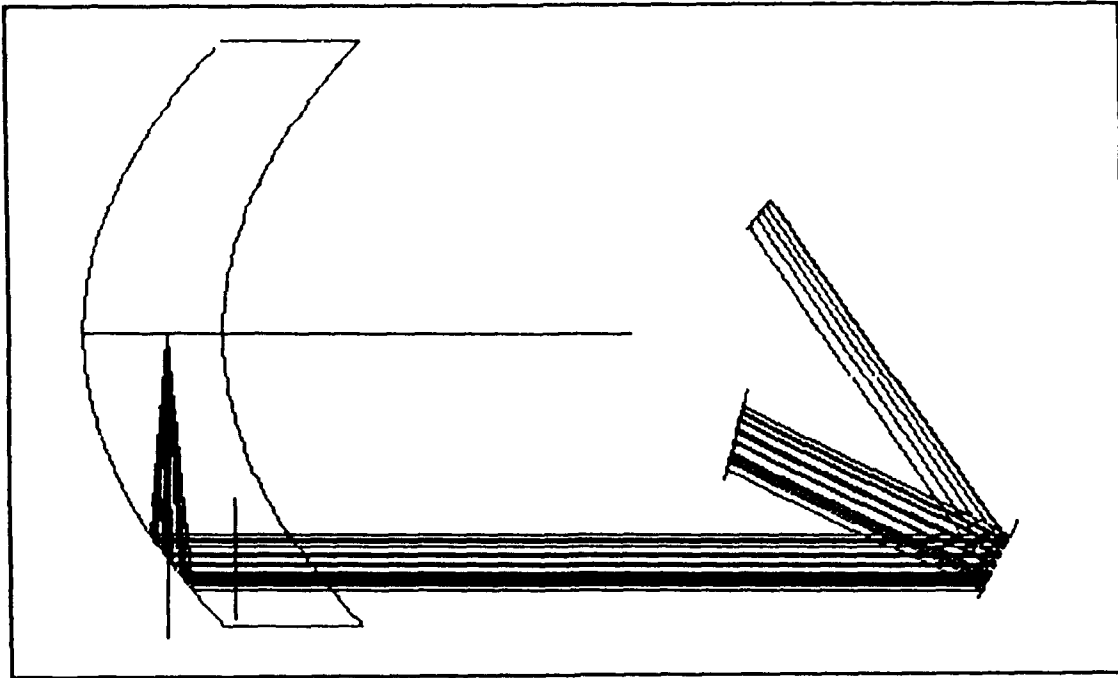


Figure 12 AMI DART Layout and Ray Trace of the Minus-One-Order Path

#### D. AMI MODEL VALIDATION AND OPTIMIZATION

The steps taken to validate the AMI design were divided into five major sets of DART interference runs. The first set was performed using an ideal point source aperture. Runs were completed using both monochromatic and multiple wavelength sources. The aperture was then altered by offsetting the source from the focus of the off-axis parabola. A "real point source" was then used in the simulation in order to note the effects of using a realistic optical pinhole at the focus of the off-axis parabola. This is the element most likely to be used in the actual construction of the AMI (Risley, 1993). The pinhole was then elongated to form a slit, another viable option for the actual instrument. Finally, the ideal point source was again used for runs conducted to simulate the input of an emission line profile.



## 1. Ideal Point Source with Monochromatic Incident Light

An ideal point source was entered as the aperture of the DART parameter file by setting all aperture dimensions equal to zero and selecting an opening one point across in both the X and Y directions. It was first verified that an input wavelength equal to the tuned wavelength ( $\lambda = \lambda_0 = 1304 \text{ \AA}$ ) produced no fringe pattern. Although there were no fringes visible on the interferogram, the wavelength domain was examined to ensure that no peaks were present. That was indeed the case. Numerous values of  $\Delta\lambda$  were then entered and the results examined. Of specific interest were the minimum and maximum allowed values of  $\Delta\lambda$  which could be determined through analysis of the fourier transformed interference patterns.

The first example demonstrates a typical interference pattern and profile along with the resulting fourier spectrum. Figures 13 through 15 show the resulting interferogram, interference profile, and FFT spectrum, respectively, for an incident wavelength of  $1304.015 \text{ \AA}$ . The minima in the interference profile are at zero and therefore the profile is not centered about the x-axis. This produces a large DC term at  $\lambda_0$  in the fourier plot, which is present in Figure 15. This interference run was conducted using a block of 400 by 400 rays sent from the aperture toward the off-axis parabola. Figures 16 through 18 show the same data using a 120 by 120 ray aperture to demonstrate the decrease in the "signal-to-noise" ratio that results from using a smaller number of rays. All subsequent ideal point source plots use a 400 x 400 ray aperture unless otherwise labeled.

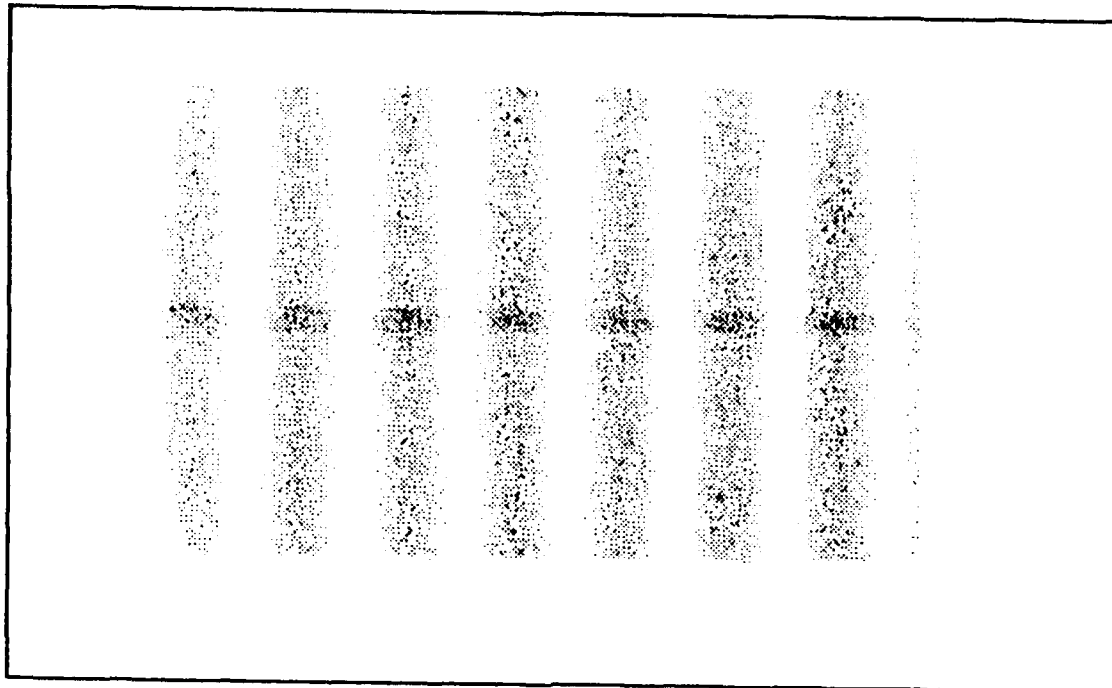


Figure 13 Ideal Point Source Interferogram for 1304.015 Å (400 x 400 rays)

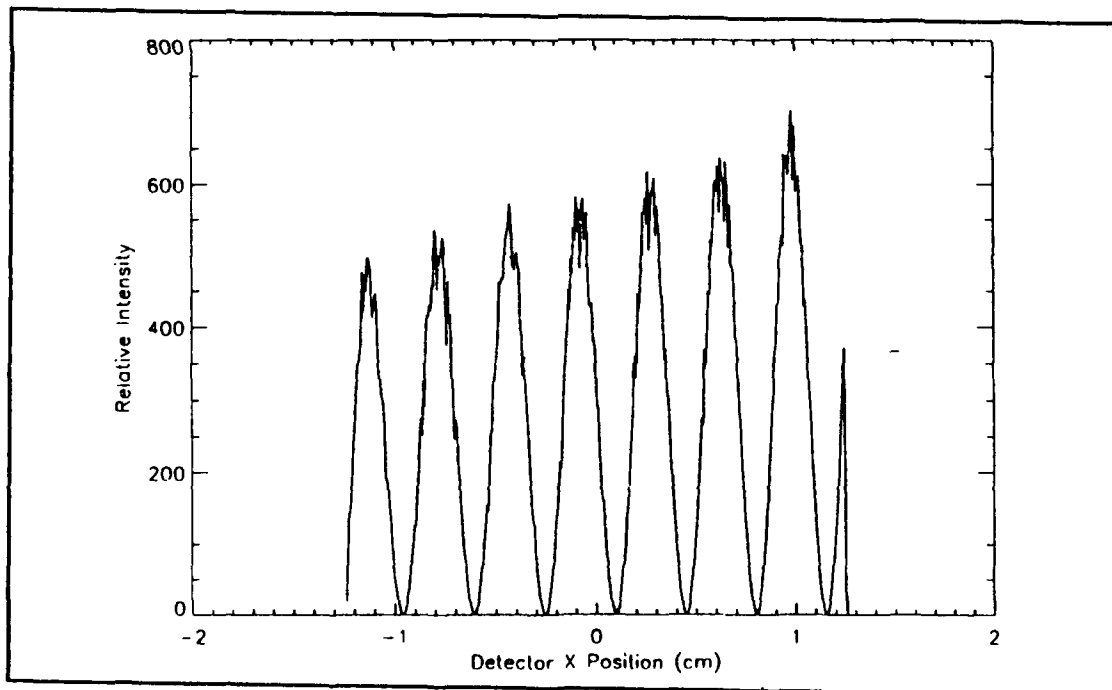


Figure 14 Ideal Point Source Interference Profile for 1304.015 Å (400 x 400 rays)

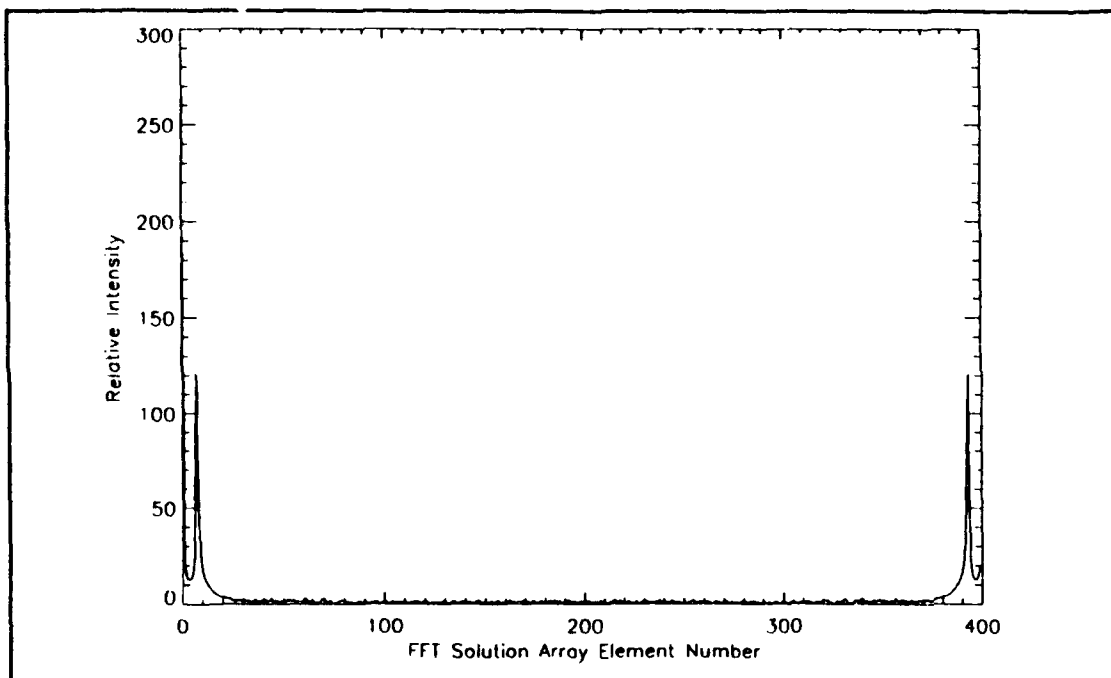


Figure 15 Ideal Point Source FFT Spectrum for 1304.015 Å (400 x 400 rays)

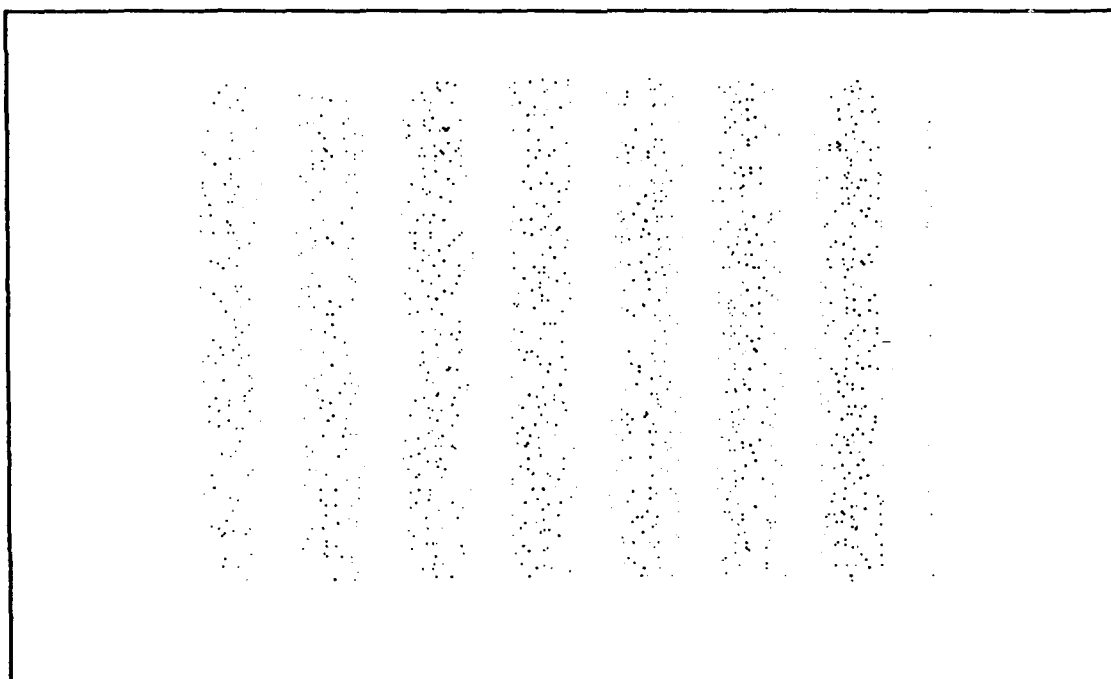


Figure 16 Ideal Point Source Interferogram for 1304.015 Å (120 x 120 rays)

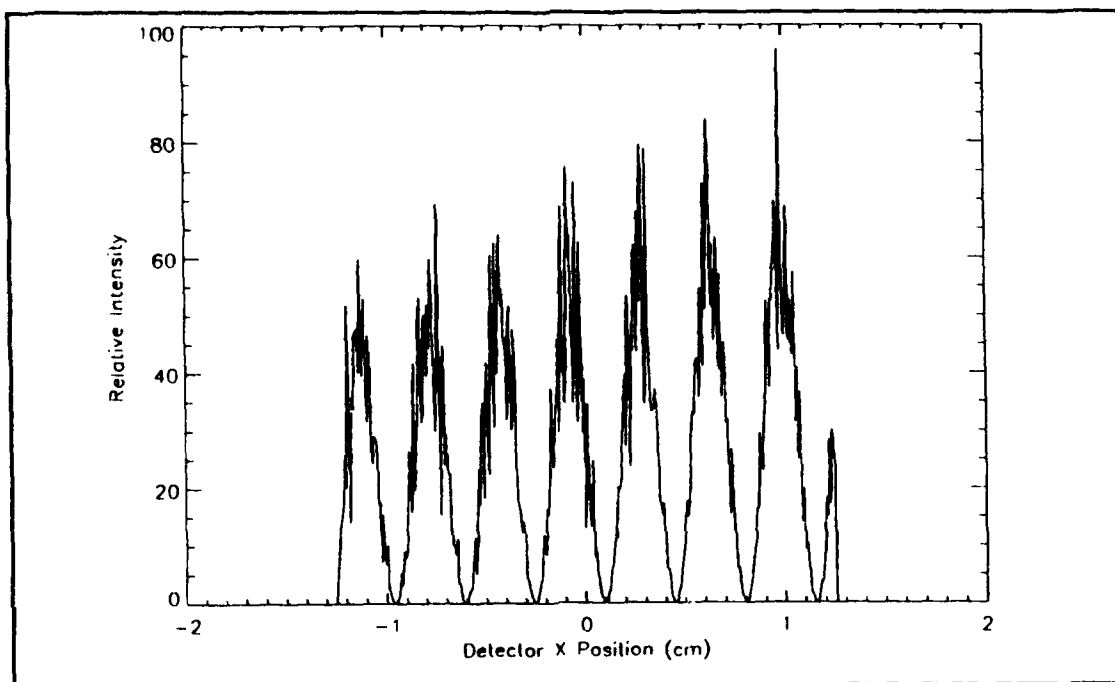


Figure 17 Ideal Point Source Interference Profile for 1304.015 Å (120 x 120 rays)

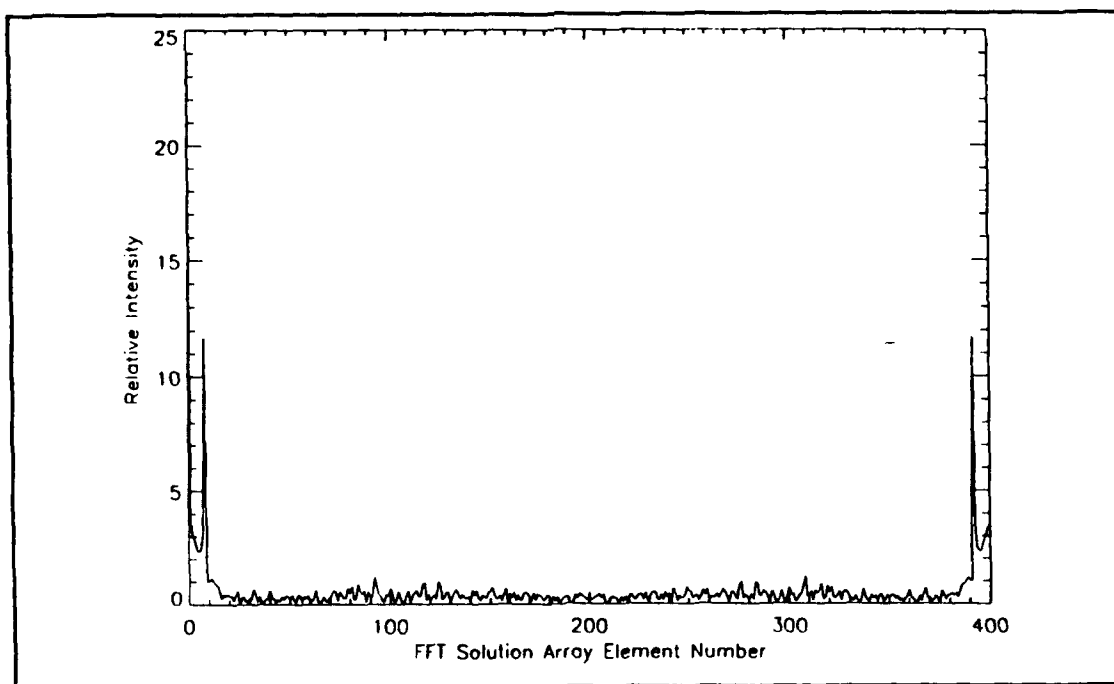


Figure 18 Ideal Point Source FFT Spectrum for 1304.015 Å (120 x 120 rays)

The next series of results, shown in Figures 19 through 21, demonstrates interference using a value of  $\Delta\lambda$  near the center of the expected bandwidth of the instrument ( $\lambda = 1304.200 \text{ \AA}$ ,  $\Delta\lambda = 200 \text{ m\AA}$ ). The interference profile has been altered by subtracting the average intensity of the entire fringe pattern from each point in the profile. This eliminates much of the DC component of the Fourier transform as can be seen in Figure 21 (indicated by "DC removed" in the figure caption). FFT spectra will now be shown as uncalibrated wavelength spectra as described above.

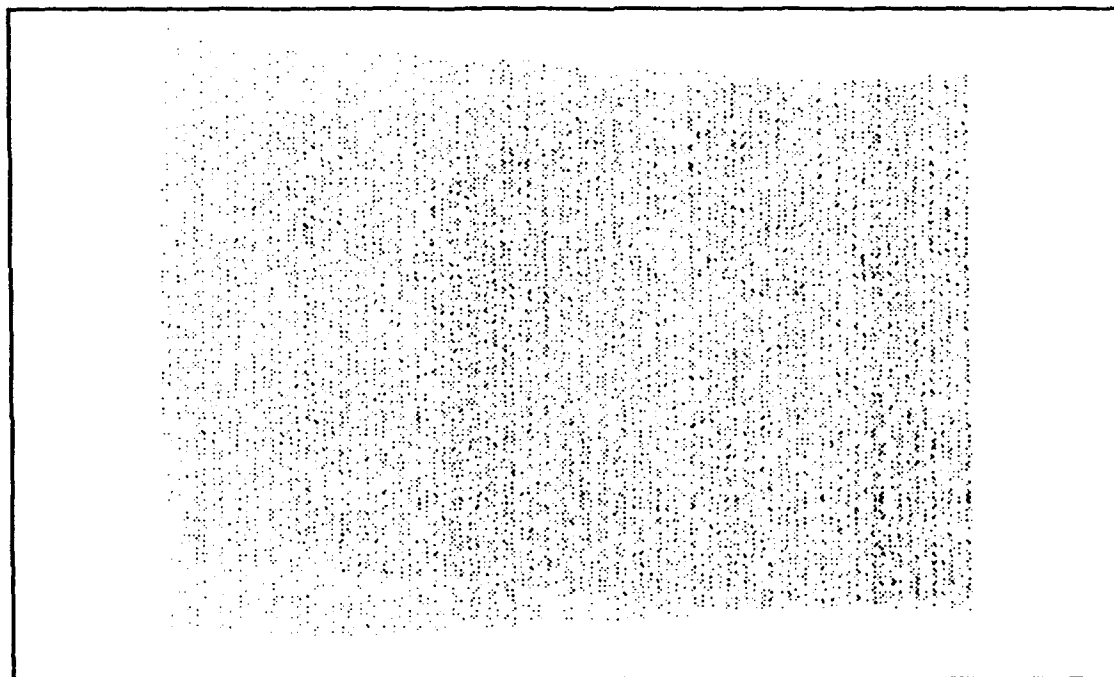


Figure 19 Ideal Point Source Interferogram for 1304.200  $\text{\AA}$

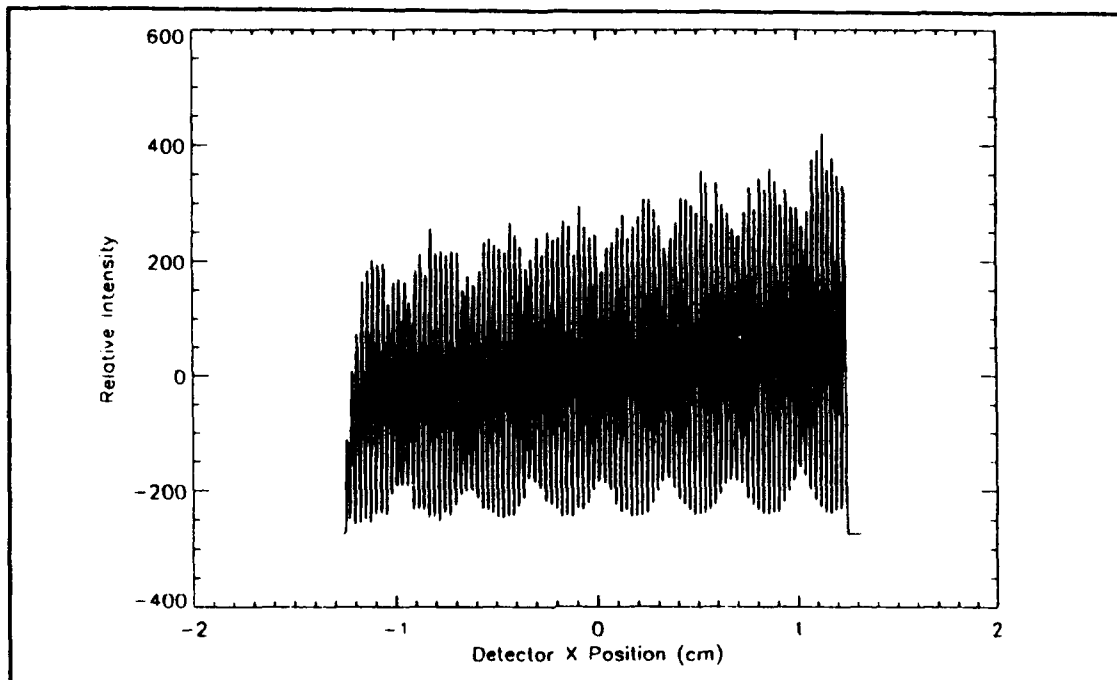


Figure 20 Ideal Point Source Interference Profile for 1304.200 Å (DC removed)

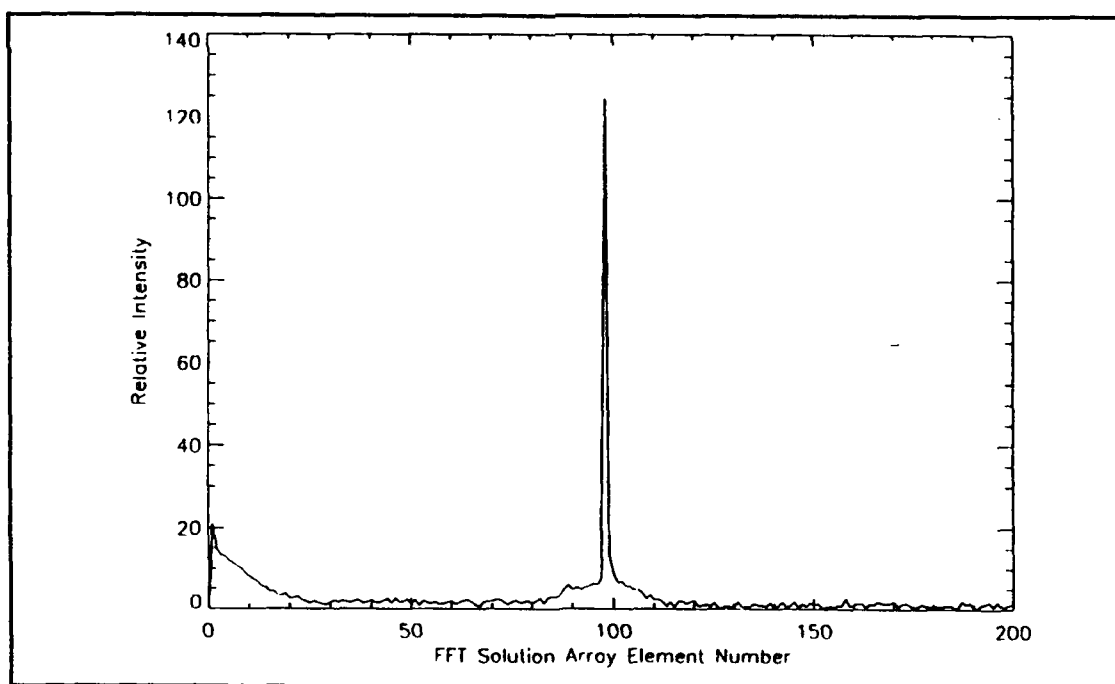


Figure 21 Ideal Point Source Wavelength Spectrum for 1304.200 Å (DC removed)

The next series of results (shown in Figures 22 and 23) gives an interference profile and wavelength spectrum for an incident wavelength near the maximum allowed wavelength of the instrument. The FFT function produces an ambiguous result when the wavelength increases beyond the maximum allowed wavelength. This ambiguity is caused by contamination of the wavelength peak due to FFT aliasing and is well understood. By noting when the aliasing begins, the maximum wavelength of the instrument can be determined.

At this point, sufficient runs had been conducted at known wavelengths to roughly calibrate the horizontal axis of the wavelength spectrum. The wavelength axis was calibrated by correlating the pixel position of peaks obtained on the wavelength spectrum with the known wavelengths that produced them. The pixel corresponding to zero spatial frequency (the zero position on the FFT spectrum) was labeled as  $\lambda_0$ . A linear relationship between FFT pixel spacing and wavelength was assumed for this project. A more accurate calculation of the pixel spacing as a function of wavelength will be required for the working prototype and flight-qualified versions of the AMI. Figure 24 shows the wavelength spectrum for an ideal point source at  $\lambda = 1304.380 \text{ \AA}$  with the wavelength axis calibration in place.

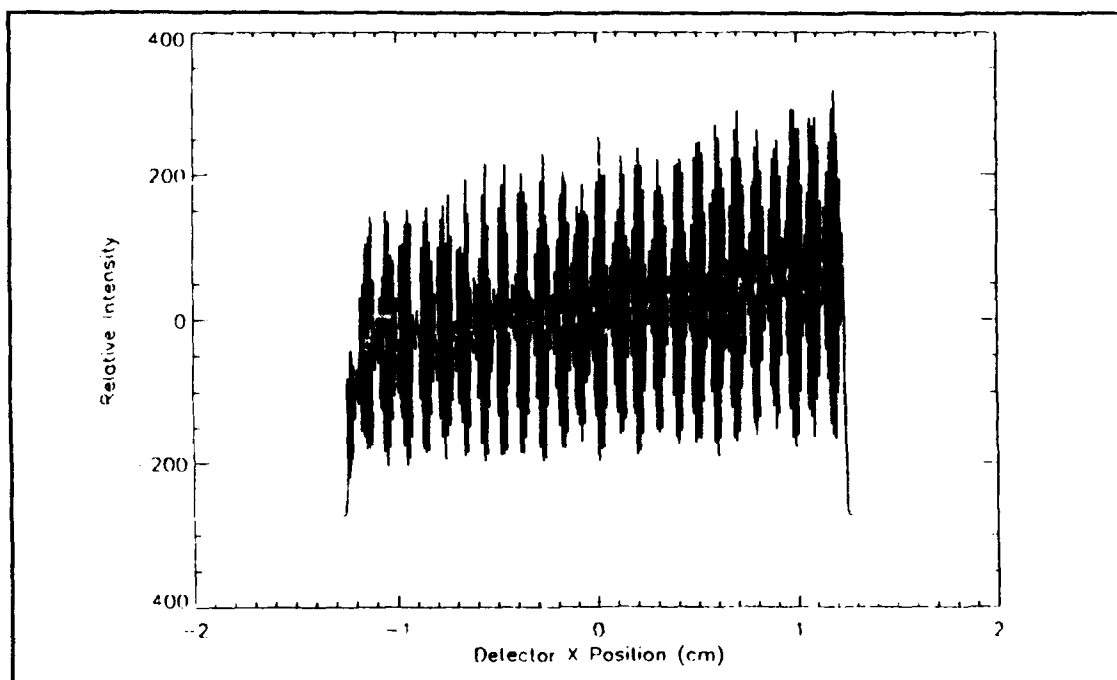


Figure 22 Ideal Point Source Interference Profile for 1304.380 Å

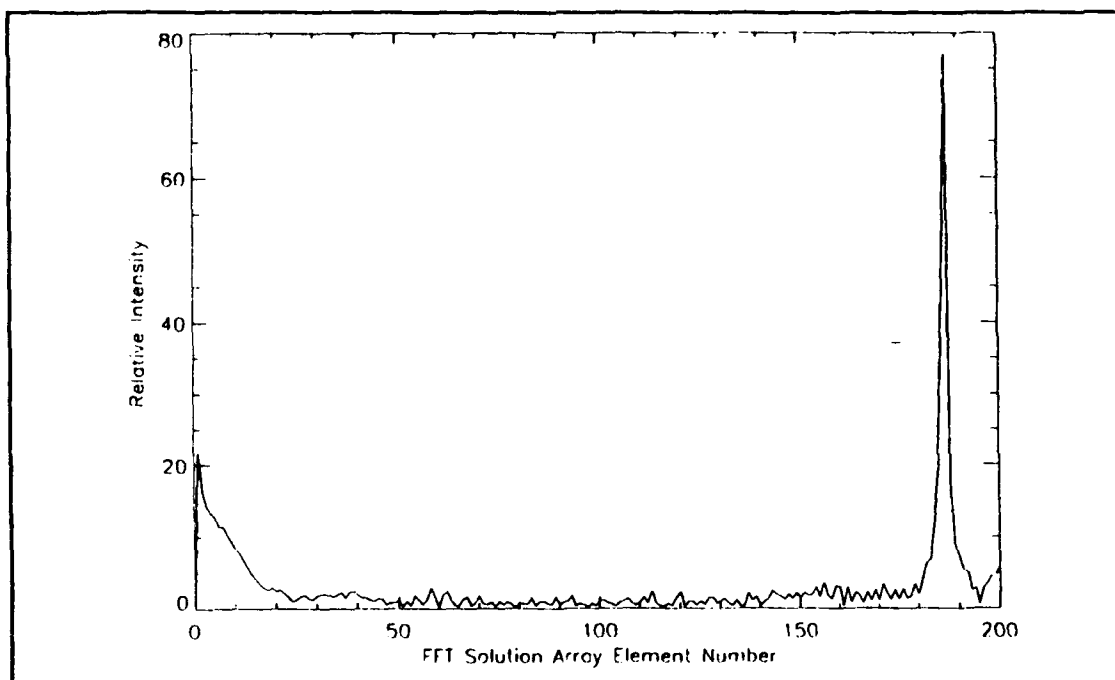


Figure 23 Ideal Point Source Wavelength Spectrum for 1304.380 Å



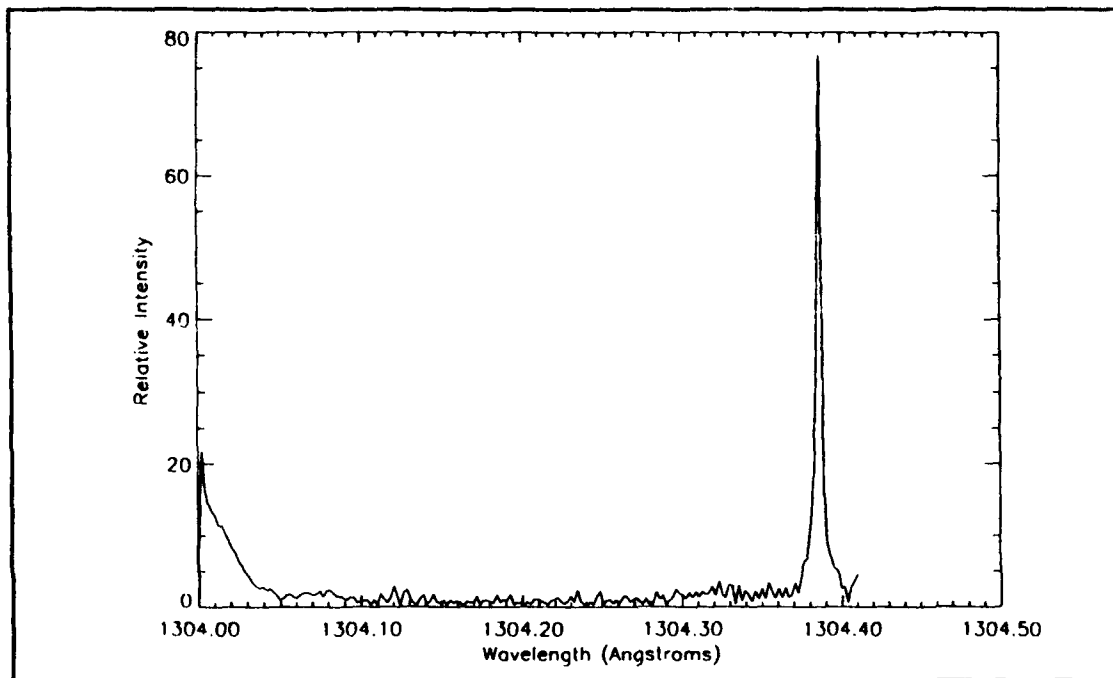


Figure 24 Ideal Point Source (Calibrated) Wavelength Spectrum for 1304.380 Å

Several interference runs were conducted as described above to more accurately pinpoint the maximum and minimum allowed values of  $\Delta\lambda$ . These values were found to be

$$\Delta\lambda_{MAX} = 400\text{m}\text{\AA} \quad (35)$$

and

$$\Delta\lambda_{MIN} = 3\text{m}\text{\AA} . \quad (36)$$

## 2. Ideal Point Source with a Multiple Wavelength Light Source

After the minimum and maximum allowed values of  $\Delta\lambda$  were found and an accurate wavelength calibration scale introduced, a light source consisting of two distinct wavelengths was modeled in order to determine the resolution of the instrument. The resolution here is considered to be the minimum separation between two wavelengths such that each individual peak in the fourier domain is recognizable. The interferogram result-

ing from two equal-intensity wavelengths is shown in Figure 25. Figures 26 and 27 show the resulting interference profile and wavelength spectrum. In the Interferogram and interference profile, two separate spatial frequencies are readily discernible. In the wavelength spectrum in Figure 27, both wavelength peaks are distinct.

Figures 28 through 31 show the wavelength spectra resulting from pairs of wavelengths near  $1303.800 \text{ \AA}$  separated by gradually decreasing wavelength differences. The wavelengths became indistinguishable when the resolution of the instrument was reached. As can be seen in Figure 30, the approximate resolution is  $4.0 \text{ m\AA}$ . By conducting several series of runs at different wavelengths, it was found that the resolution is roughly constant throughout the bandpass of the instrument.

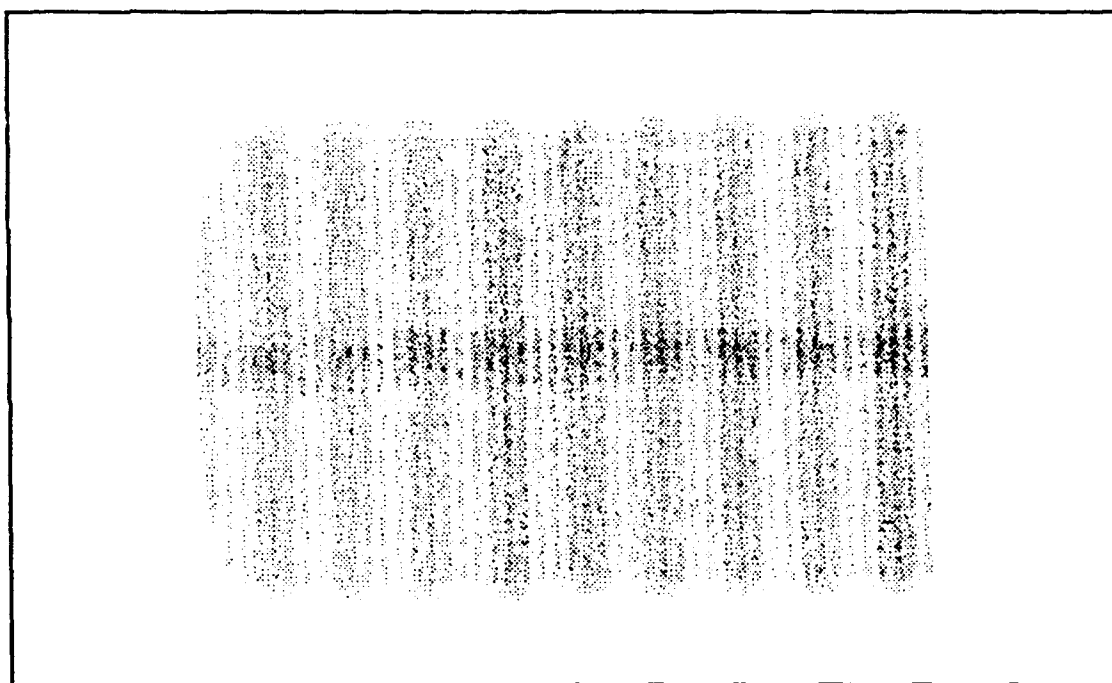


Figure 25 Ideal Point Source Interferogram for  $1303.980 \text{ \AA}$  and  $1303.900 \text{ \AA}$

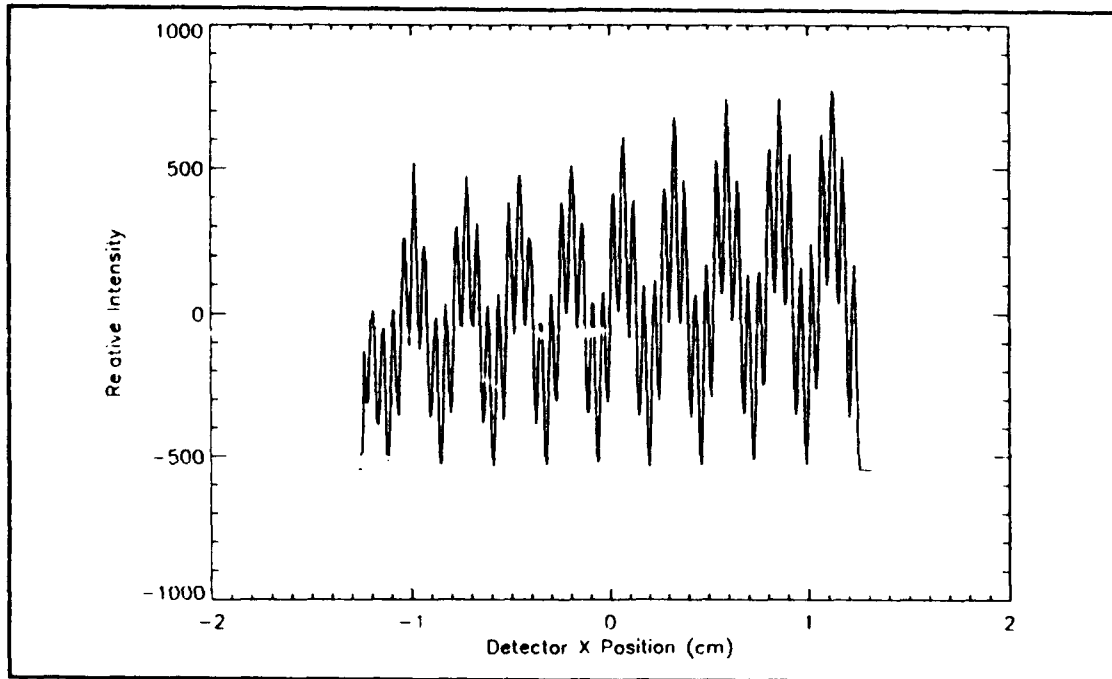


Figure 26 Ideal Point Source Interference Profile for 1303.980 Å and 1303.900 Å

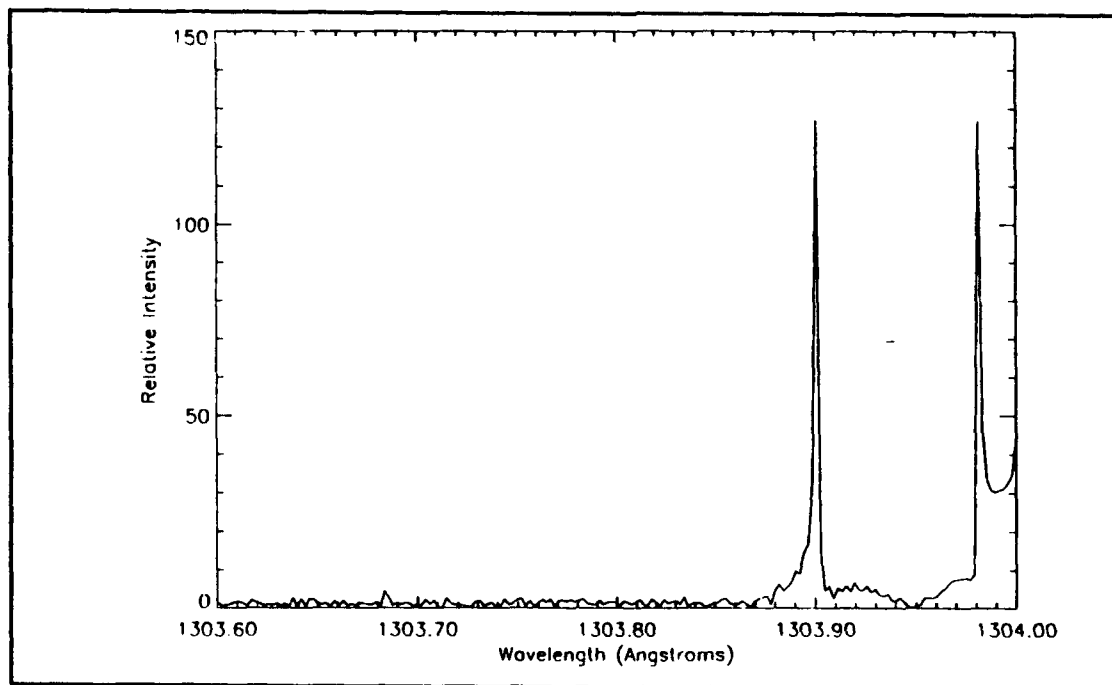


Figure 27 Ideal Point Source Wavelength Spectrum for 1303.980 Å and 1303.900 Å

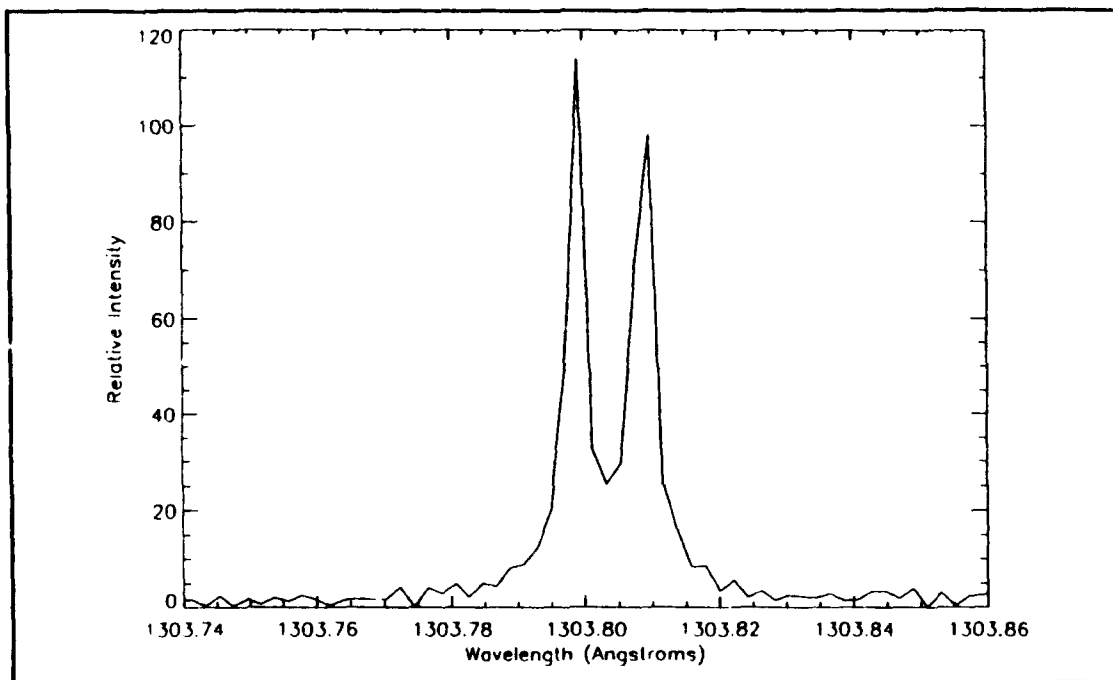


Figure 28 Ideal Point Source for 1303.810 and 1303.800 Å ( $\Delta\lambda = 10 \text{ mÅ}$ )

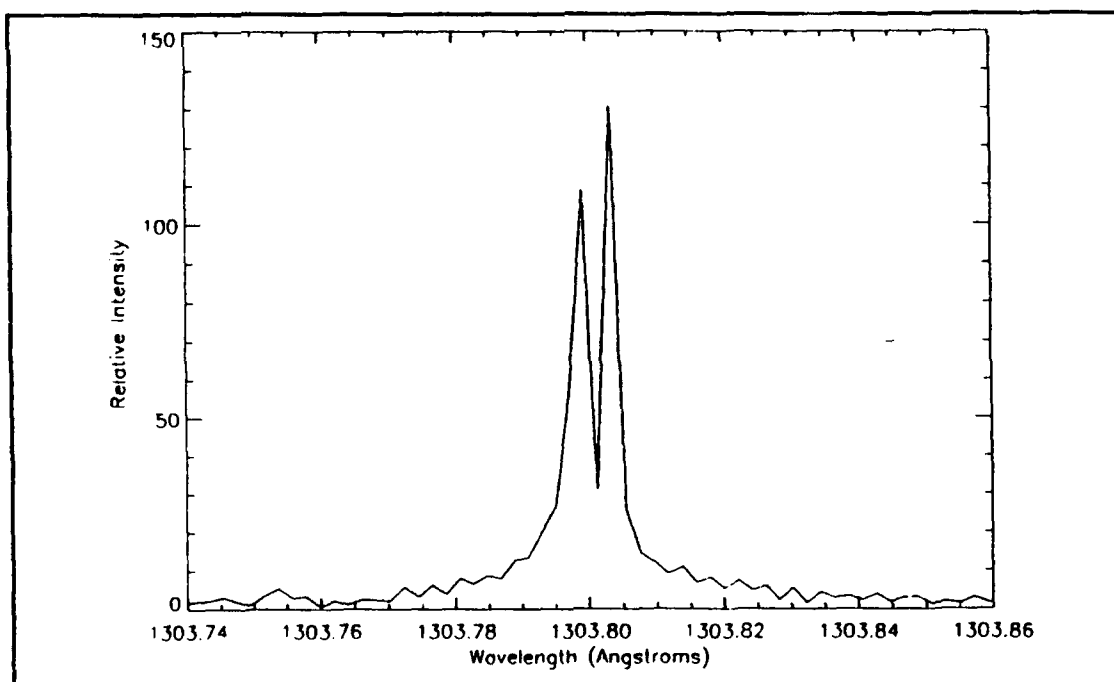


Figure 29 Ideal Point Source for 1303.805 and 1303.800 Å ( $\Delta\lambda = 5 \text{ mÅ}$ )

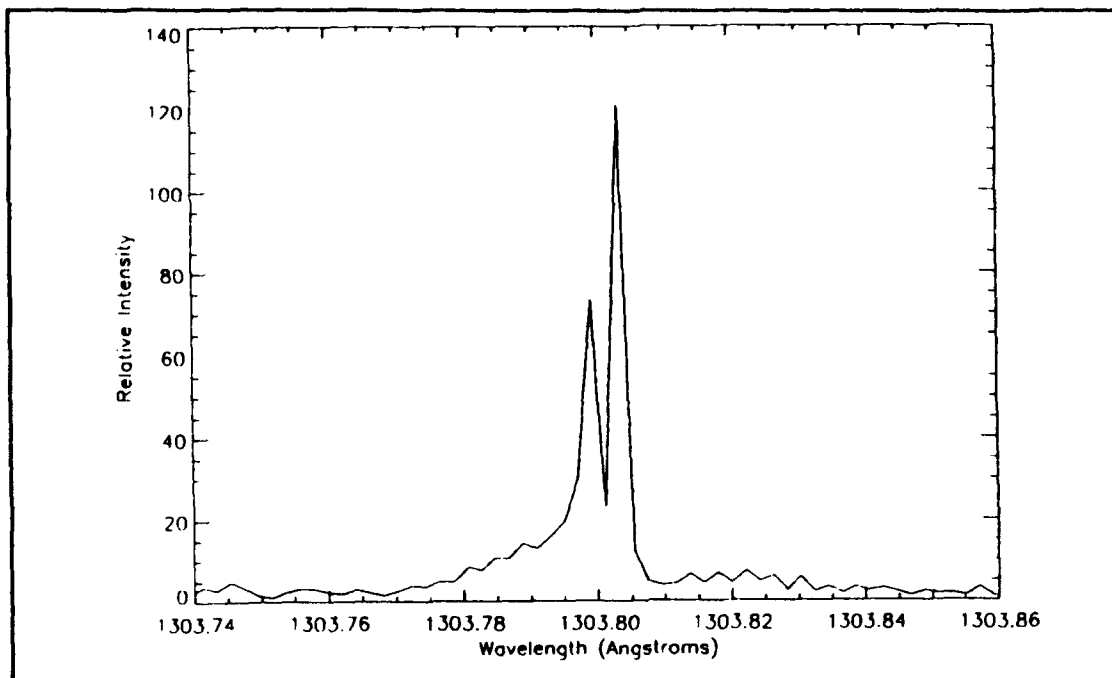


Figure 30 Ideal Point Source for 1303.804 and 1303.800 Å ( $\Delta\lambda = 4 \text{ mÅ}$ )

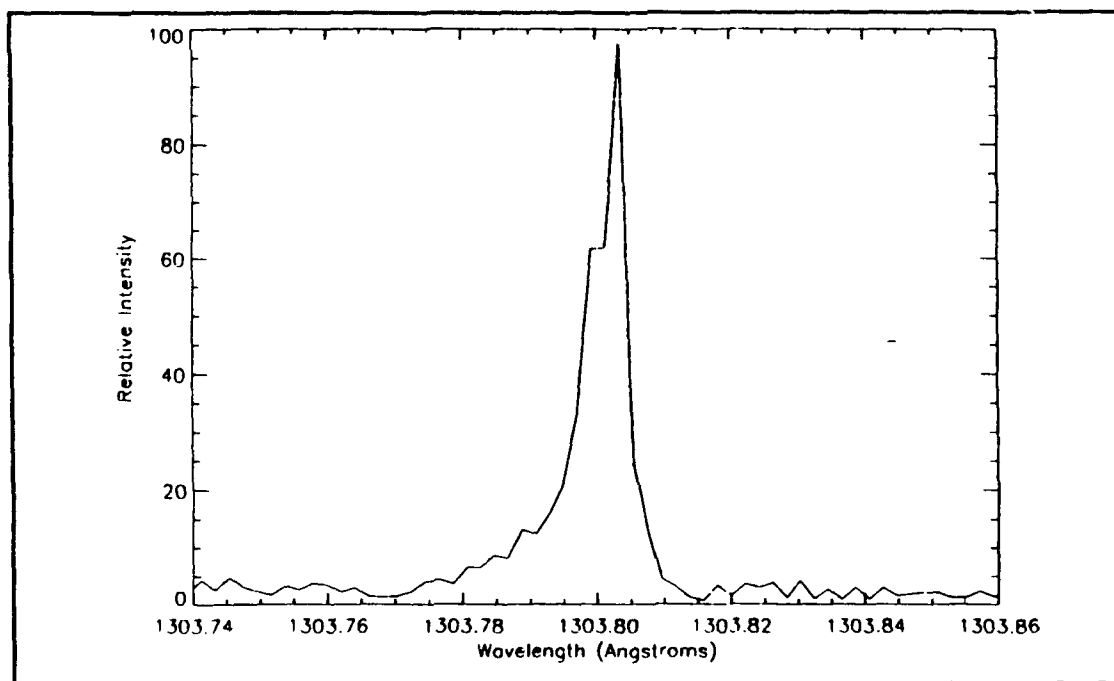


Figure 31 Ideal Point Source for 1303.8035 and 1303.8000 Å ( $\Delta\lambda = 3.5 \text{ mÅ}$ )

### 3. Offset Ideal Point Source

Several interference runs were conducted using a point source offset slightly from the focus of the parabola. Offsets up to  $250\ \mu\text{m}$  in the negative X direction were used. These runs were made on the AMI version containing larger than realistic elements so that all rays exiting the mask of the parabola would strike the detector. In this way, the effect of the offset could be observed without the loss of rays that would occur with smaller components. It was discovered that offsets greater than approximately  $100\ \mu\text{m}$  caused noticeable curvature of the fringes. An example of the fringe pattern caused by an ideal point source offset  $250\ \mu\text{m}$  from the focus is shown in Figure 32. This curvature caused a deterioration of the interference profile since the fringes were no longer parallel with the vertical summing bins used by DART, making the FFT peak much less pronounced. The curvature in the fringe pattern will later be used to help explain the effect of a pinhole on the interference patterns.

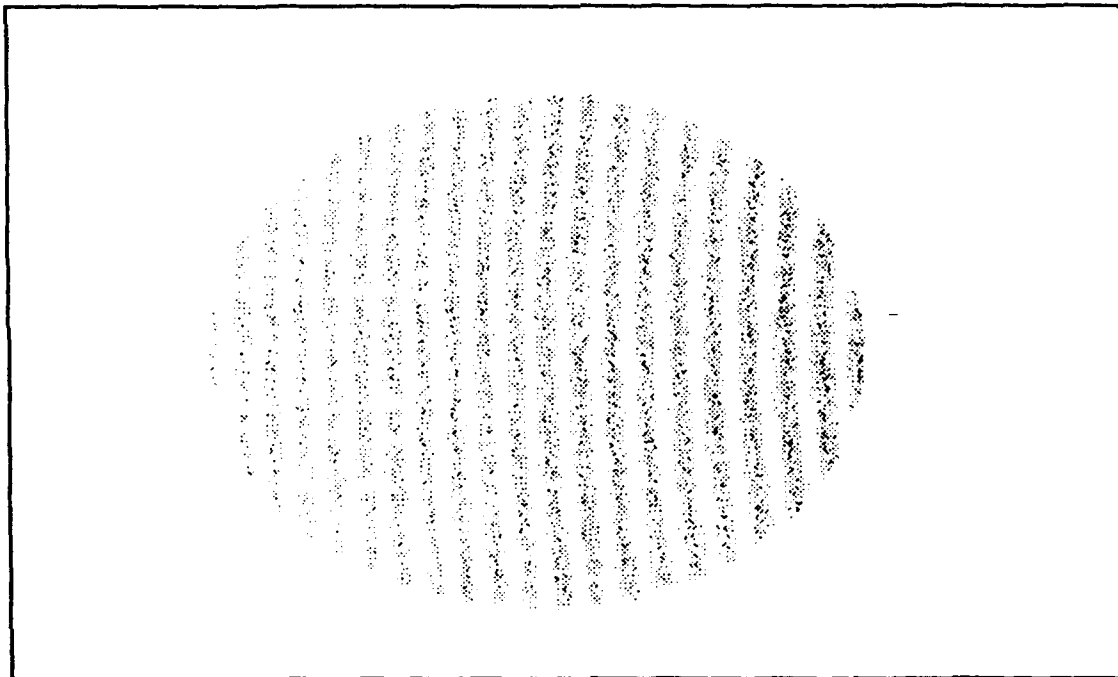


Figure 32 Ideal Point Source (Offset  $250\ \mu\text{m}$ ) Interferogram for  $1304.015\ \text{\AA}$

#### 4. Pinhole Source

The effect of a pinhole source on interference is the eventual washing out of fringe patterns caused by overlapping fringes from multiple rays separated at the source. Like the offset point source, the pinhole interference runs were conducted on the large element AMI simulation. Circular pinholes were used with diameters of 100, 250 and 500  $\mu\text{m}$  (corresponding to commercially available sizes). Figures 33 through 35 show interferograms for these pinhole diameters. The 100  $\mu\text{m}$  pinhole produced an interferogram nearly identical to that of the ideal point source. All fringes were distinct and showed high contrast. The interferogram for the 250  $\mu\text{m}$  pinhole had a fringe contrast that was noticeably lower than the 100  $\mu\text{m}$  case. Fringes became almost completely washed out and indistinguishable using the 500  $\mu\text{m}$  source. Figures 36 and 37 show the interference profile and wavelength spectrum for a pinhole diameter of 500  $\mu\text{m}$ . Although the wavelength peak is visible in Figure 37, it is less pronounced than that obtained with the ideal point source or with smaller pinholes.

While conducting this analysis, it became apparent that the distance between optical elements in the instrument design is a major factor contributing to the washout effect. The sensitivity of the instrument to fringe pattern washout is believed to be proportional to the overall path length of each beam. In the present case, where the instrument modeled has an especially large grating-to-parabola distance (60 cm), the washout effect was severe. Additionally, distances between the grating and the mirrors were larger than necessary in this instrument, compounding the effects of fringe washout. Although not verified, it is expected that shorter distances between the elements would lessen the detrimental effects of the size of the pinhole. Minimizing the distance between optical elements is not expected to adversely affect instrument resolution or bandpass.

It should be pointed out that anomalous results were obtained when the AMI was modeled with smaller more realistic-sized elements (25 mm diameter mirrors with a 25x10 mm detector). The fringes for this case were strangely indiscernible, even with the 100  $\mu\text{m}$  source. Although the cause of this is not fully understood, it is suspected that an inadvertent error in the construct of the parameter files contributed to the poor results obtained.

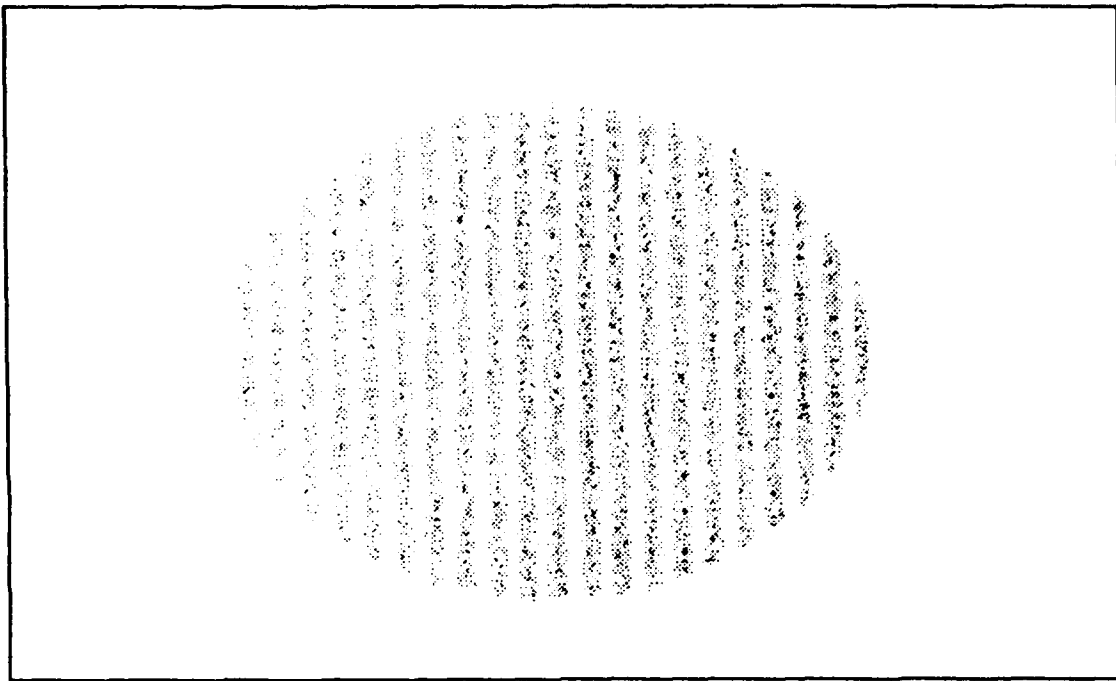


Figure 33 100  $\mu\text{m}$  Diameter Pinhole, Interferogram for 1304.015  $\text{\AA}$



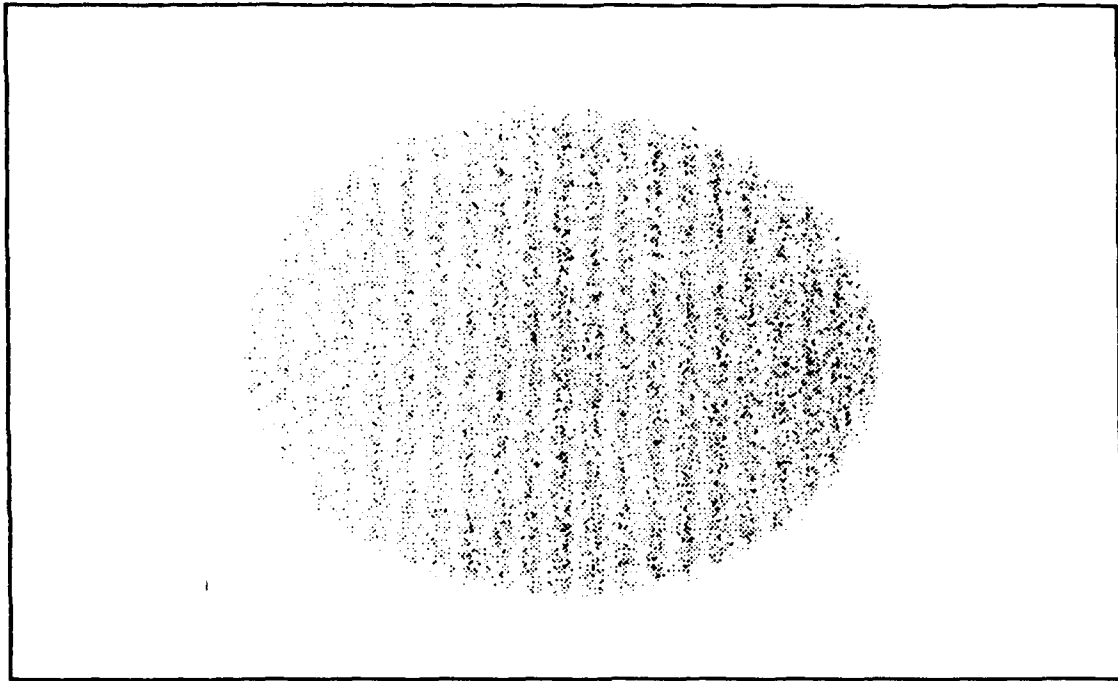


Figure 34 250  $\mu\text{m}$  Diameter Pinhole, Interferogram for 1304.015  $\text{\AA}$

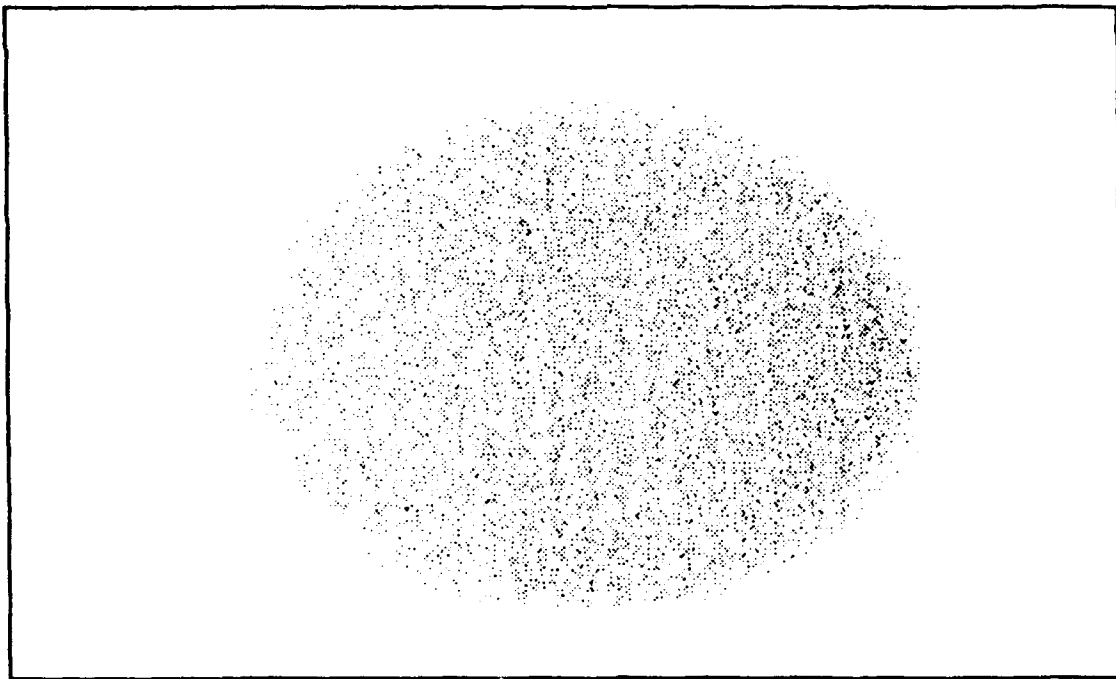


Figure 35 500  $\mu\text{m}$  Diameter Pinhole, Interferogram for 1304.015  $\text{\AA}$

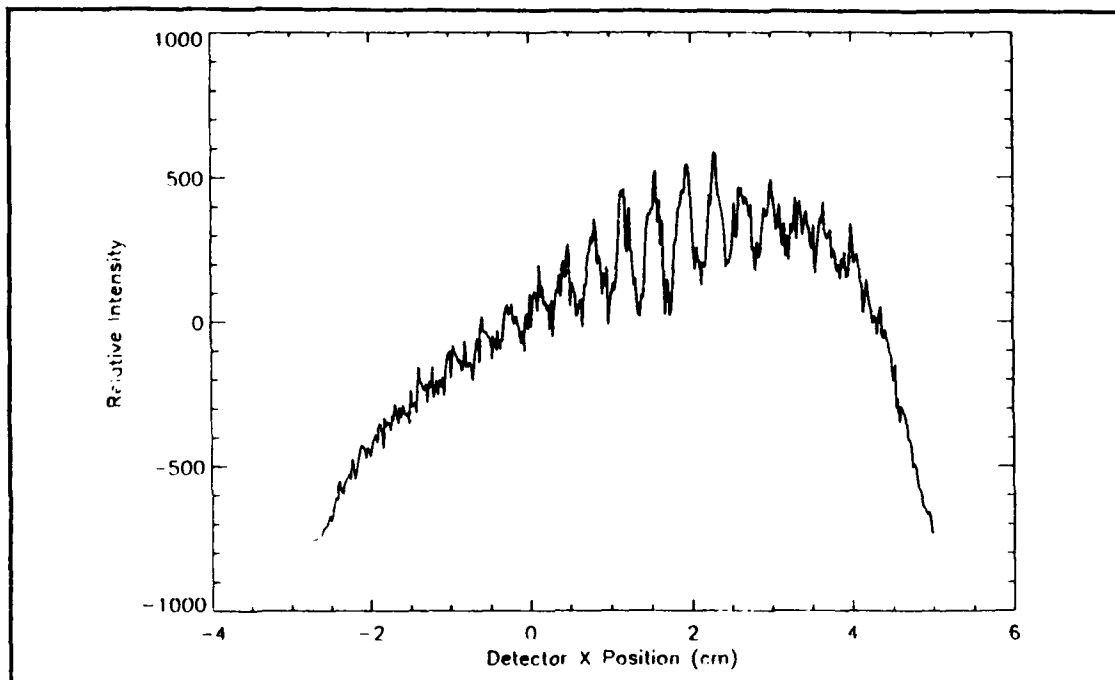


Figure 36 500  $\mu\text{m}$  Diameter Pinhole, Interference Profile for 1304.015  $\text{\AA}$

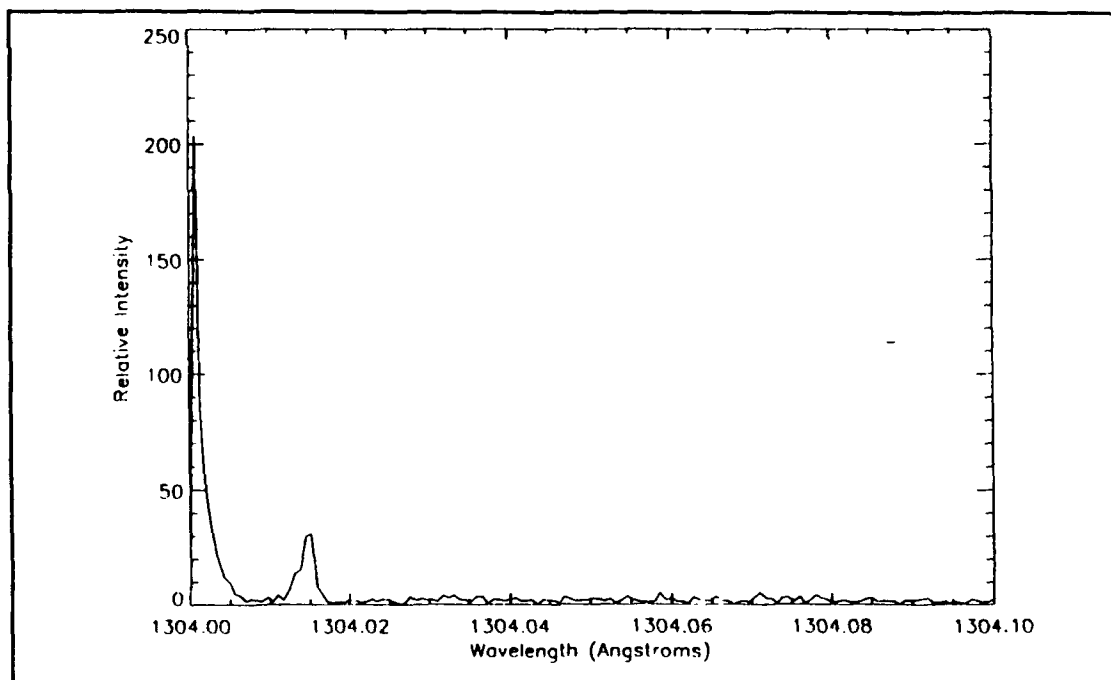


Figure 37 500  $\mu\text{m}$  Diameter Pinhole, Wavelength Spectrum for 1304.015  $\text{\AA}$

## **5. Slit Source**

The final source presented is the "real line source" or slit source. This was examined to determine the effect on interference patterns from the use of commercially available slits at the instrument aperture. It was discovered that the horizontal dimension of the slit produces instrument behavior similar to that of the pinhole. The vertical dimension of the slit had little effect on performance. Therefore, the AMI designer should make the choice between the use of a slit or pinhole based on intensity requirements at the detector. Slit or pinhole dimensions should be made based on the trade-off between decreased fringe contrast and increased intensity. Provided sufficient light is available at the detector, maximum sharpness of fringes can be obtained through the use of pinholes with diameters of 100  $\mu\text{m}$  or smaller.

## **6. Other Results**

Other results obtained throughout the course of this research include the effect of grating angle of incidence on instrument resolution. Several interference runs were performed using the interferometer portion of the spectrograph alone using a collimated beam. It was discovered that as long as the instrument parameters were accurately calculated for the desired tuned wavelength, resolution was not significantly affected by the angle of incidence. Therefore, the angle of incidence should be optimized based on instrument form, fit, and function requirements rather than instrument resolution desires.

## **E. OXYGEN 1304 Å LINE PROFILE INTERFERENCE**

### **1. Profile Modeling**

The solar OI 1304 Å triplet profile was simulated using the method of Gladstone (1992) discussed above. The profile for the 1304 Å line was modelled using the IDL procedure PROF.PRO and the accompanying function MODEL1.PRO, both included in

Appendix A. As this thesis is only concerned with a proof-of-concept, the simulation used only a representative set of values for the line integrated flux,  $x$ -offset, and  $x$ -dispersion from those given by Gladstone for  $\lambda_0 = 1304 \text{ \AA}$ . The IDL procedure first converts  $x$ -offset and  $x$ -dispersion from Doppler velocity to wavelength using Equations (8) and (9) and then calculates the flux as a function of wavelength using Equation (7). The procedure then plots the profile intensity versus wavelength. Additional IDL procedures were written to write the profile data to both postscript files for later printing and data files for translation into DART. These IDL procedures are also contained in Appendix A.

A representative  $1304.86 \text{ \AA}$  line profile simulation is shown in Figure 38 below for  $\pi F = 3830 \text{ ergs cm}^{-2} \text{ sec}^{-1}$ ,  $x_{\text{dis}} = 10.6 \text{ km sec}^{-1}$ , and  $x_{\text{off}} = 9.5 \text{ km sec}^{-1}$ .

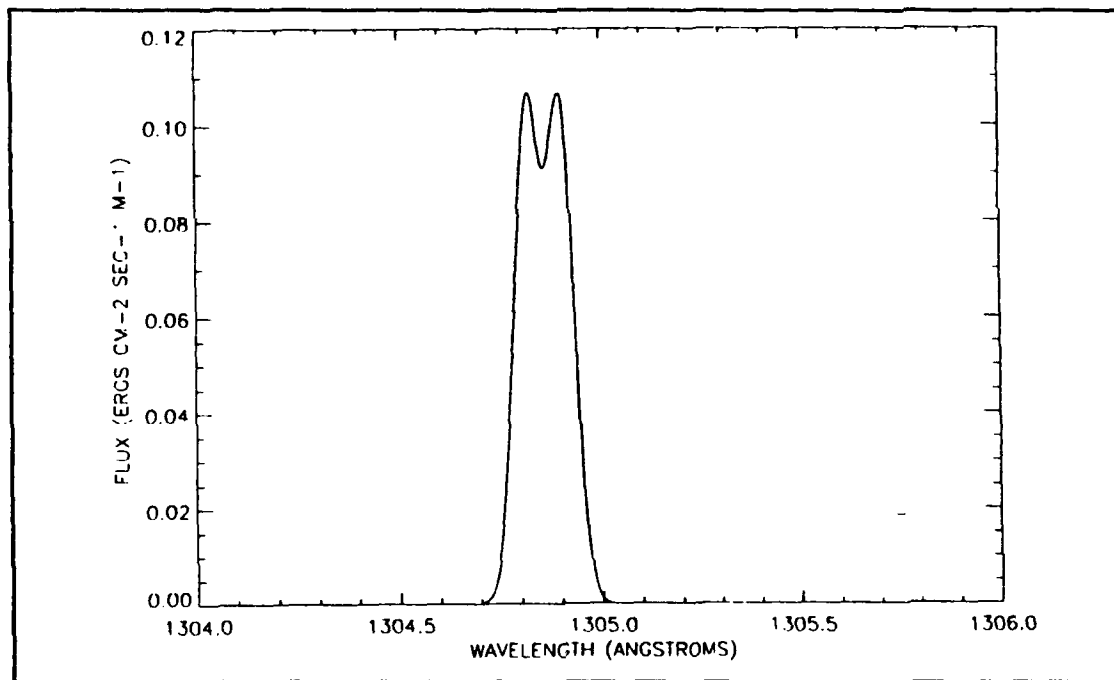


Figure 38 Solar Oxygen  $1304 \text{ \AA}$  Triplet Line Profile Simulation (after Gladstone (1992))

## 2. $1304 \text{ \AA}$ Line Profile Interference Results

The final set of interference runs was conducted using an incident light source consisting of multiple wavelengths to simulate the effects of the atomic oxygen triplet pro-

file at 1304 Å. As an initial test, one side of the emission line profile of Figure 38 above was modeled by creating an array of wavelength versus intensity values using from five to 150 array elements. These data points were entered into the DART program as multiple wavelengths of varying intensity. As all relative intensities in DART must be entered as integers, the intensity values of the line profile were scaled and truncated. When the wavelength interval between data points was larger than the instrument resolution, the wavelength spectra from the resulting interference showed distinct peaks for each wavelength. Although there were gaps between the peaks, the outline of the peaks resembled the shape of the line profile simulated. As more points were added, nearing the instrument resolution, the size of the gaps decreased but there was substantial noise and a large DC component present. When the number of points in the model was increased so that the interval between data points was less than the instrument resolution, the shape of the line profile became indistinct. This was due to the presence of a low frequency noise component. As greater numbers of points in the simulation were added, the FFT spectra did not improve.

In order to minimize the effect of the low frequency contamination in the fourier domain, the line profile was offset from  $\lambda_0$ . The value selected for the center of the new line profile was 1303.8 Å. This offset had the effect of modeling a new instrument with a tuned wavelength over 200 mÅ higher than the wavelength of interest. With this change, wavelength spectra more accurately represented the incident emission line profile. The line profile was reproduced particularly well when the input profile was compressed along the wavelength axis to make it narrower. In this way, an entire line profile could be entered with wavelength spacing smaller than the pixel spacing of the instrument, while requiring that fewer than 100 wavelength values be entered in DART. Fewer wavelengths at the DART aperture tended to make the application run more quickly and with fewer errors. An example of the compressed (and offset) line profile is shown in Figure 39. The resulting interference profile and wavelength spectrum are shown in Figures 40 and 41, respec-

tively. As can be seen in Figure 41, the profile in the wavelength spectrum closely resembles that of the incident profile. Of note is the accuracy of the relative spacing of the peaks and the depth of the self-reversal in the reproduced profile. The values used in modeling the profile displayed in Figure 39 are given in Table III. For this simulation only 50 wavelength bins were used. It should be pointed out that the quality of the line profile recovered by this technique (Figure 41) improves proportionately with the number of wavelength bins. Due to limitations in the current computer setup, however, attempts to increase this number were not successful.

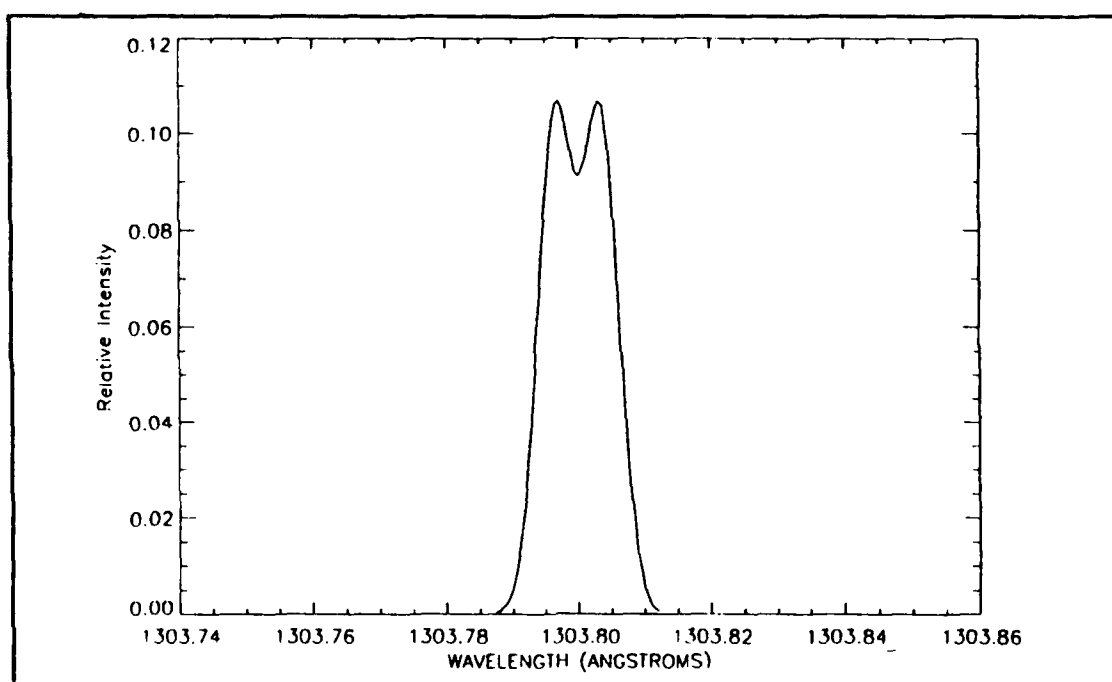


Figure 39 Offset and Compressed Line Profile Centered at 1303.8 Å

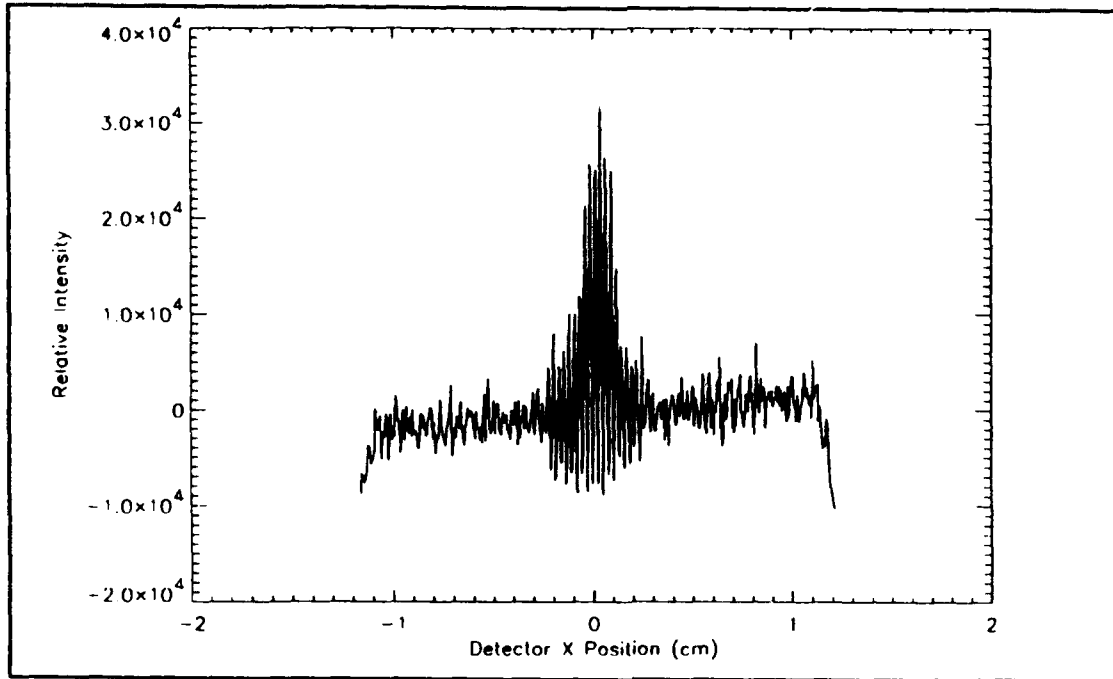


Figure 40 Interference Profile for the Line Profile of Figure 39

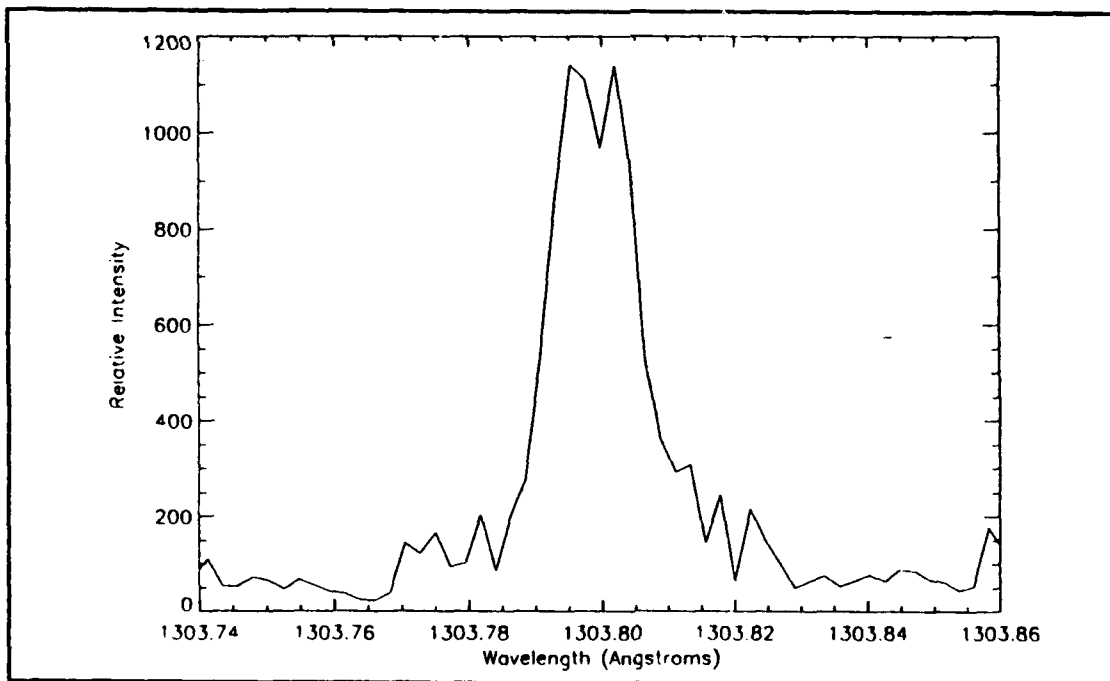


Figure 41 Wavelength Spectrum of the Line Profile of Figure 39

TABLE III. OFFSET LINE PROFILE DATA POINTS

Relative Intensity	Wavelength (Å)	Relative Intensity	Wavelength (Å)	Relative Intensity	Wavelength (Å)
1	1303.7885	105	1303.7965	95	1303.8046
2	1303.7891	106	1303.7970	87	1303.8051
3	1303.7896	105	1303.7975	77	1303.8055
5	1303.7900	102	1303.7980	65	1303.8060
8	1303.7905	98	1303.7985	54	1303.8065
12	1303.7910	94	1303.7991	43	1303.8070
17	1303.7915	92	1303.7994	33	1303.8075
24	1303.7921	91	1303.8000	25	1303.8080
33	1303.7925	91	1303.8004	18	1303.8086
43	1303.7931	94	1303.8010	12	1303.8090
54	1303.7935	98	1303.8016	8	1303.8096
65	1303.7941	102	1303.8020	5	1303.8099
76	1303.7944	105	1303.8026	3	1303.8105
87	1303.7950	106	1303.8030	2	1303.8109
95	1303.7955	105	1303.8036	1	1303.8115
102	1303.7960	102	1303.8040	0	1303.8120



## F. RESULTS SUMMARY

Table IV summarizes the numerical results obtained in conducting this research and represents the expected performance parameters of the AMI. The resolving power given is calculated from

$$\mathfrak{R} = \frac{\lambda}{\Delta\lambda} = \frac{1304}{0.004} = 326000 . \quad (37)$$

TABLE IV. INSTRUMENT PARAMETERS BEFORE CORRECTION

Parameter	Result
max $\Delta\lambda$	400 mÅ
min $\Delta\lambda$	3 mÅ
Bandwidth	397 mÅ
Resolution	4 mÅ
Resolving Power	$3 \times 10^5$

Pixel spacing is the wavelength spacing between elements in the FFT array. Alternatively, it can be thought of as the smallest  $\Delta\lambda$  that will produce a peak in the first FFT array position (nearest to  $\lambda_0$ ). A formula for pixel spacing, given by Wallace (1992) is

$$\Delta\lambda_{\text{MIN}} = \frac{\lambda_0}{2L} \sqrt{\frac{1}{\rho^2} - \left(\frac{\lambda_0}{2}\right)^2} , \quad (38)$$

where L is the length of the detector. Substituting the values used for this instrument into Equation (38) gives

$$\Delta\lambda_{\text{MIN}} = 4.0003 \times 10^{-13} \text{ m/pixel} \cong 4 \text{ mÅ/pixel} . \quad (39)$$

Alternatively, the pixel spacing can be found experimentally (or in this case by simulation) by dividing the demonstrated bandpass of the instrument by the number of elements in the FFT array. In the case of the AMI, the pixel spacing is

$$\Delta\lambda_{\text{MIN}} = \frac{400 \text{ m}\text{\AA}}{200 \text{ pixels}} = 2 \text{ m}\text{\AA}/\text{pixel} . \quad (40)$$

The apparent discrepancy between the expected pixel spacing and that determined by modeling the AMI can be explained by a factor-of-2 error that was recently discovered in the interference algorithm of the DART program (D. D. Cleary, private communication, 1993). Equation (23) gives the irradiance resulting from interference at a field point, P. Factoring out the 2I term, the irradiance is

$$I_{\text{P}} = 2I (1 + \cos\delta) . \quad (41)$$

Through the use of a common trigonometric identity, it becomes

$$I_{\text{P}} = 2I \cos^2 \frac{\delta}{2} . \quad (42)$$

In its interference algorithm, DART was found to have used the equation

$$I_{\text{P}} = 2I \cos^2 \delta . \quad (43)$$

This introduces a factor-of-two error in the spatial frequency of the interference calculations. This error had the effect of halving the bandwidth and the pixel resolution obtained for this instrument. Were this factor-of-two error corrected for and the interference runs repeated, the revised performance parameters would have been those given in Table V.

**TABLE V. CORRECTED INSTRUMENT PARAMETERS**

<b>Parameter</b>	<b>Result</b>
<b>max <math>\Delta\lambda</math></b>	<b>800 mÅ</b>
<b>min <math>\Delta\lambda</math></b>	<b>3 mÅ</b>
<b>Bandwidth</b>	<b>797 mÅ</b>
<b>Resolution</b>	<b>8 mÅ</b>
<b>Resolving Power</b>	<b><math>1.5 \times 10^5</math></b>

It should be emphasized that the values presented above in Tables IV and V are based on a detector length of 25 mm and a detector pixel spacing of 60  $\mu\text{m}$ . The latter is constrained primarily by a limitation in the DART program. The use of a commercially available one-dimensional array detector with a detector pixel spacing of 25  $\mu\text{m}$  could potentially improve the bandwidth and resolution.

## VI. CONCLUSIONS AND RECOMMENDATIONS

### A. SUMMARY OF FINDINGS AND CONCLUSIONS

The design of a high resolution All-reflection Michelson Interferometer for far and extreme ultraviolet atmospheric spectroscopy was studied using software ray tracing techniques. Results for various apertures and wavelengths of incident light were presented in several forms. Interferograms were presented to show fringe patterns created at the two dimensional detector. Interference profiles displayed a plot of the intensity of interfering light versus the detector horizontal axis position. Finally, so-called wavelength spectra were produced by taking the fast fourier transform of the interference profiles.

An ideal point source emanating monochromatic light at the aperture, produced high-contrast interference fringes on the interferogram and sharp peaks on the wavelength spectrum. Light of varied wavelength was used to determine the minimum and maximum allowed  $\Delta\lambda$  of the instrument and a calibrated wavelength scale was introduced for subsequent wavelength spectra. Distinct peaks were observed on the wavelength spectra for incident light consisting of two wavelengths. Spacing of the incident wavelengths was varied to determine the instrument resolution. The expected bandwidth, maximum and minimum allowed  $\Delta\lambda$ , resolving power and resolution of the instrument were thereby determined and then corrected for a factor-of-two error discovered in the ray tracing software. These results were presented in Table V.

It was found that using a pinhole or slit as the aperture at the focus of the off-axis paraboloid tended to cause a marked decrease in fringe contrast compared with that of an ideal point source. It was determined that, for the instrument modeled here, the maximum pinhole diameter for satisfactory fringe contrast was 100  $\mu\text{m}$ . It was also shown that the effect of offsetting the source of incident light from the focus of the collimating paraboloid

is to cause a curvature of the fringe pattern. This curvature is believed to be the cause of the decrease in fringe contrast for the wavelength spectrum of the pinhole source. It is also believed that the sensitivity of fringe contrast to pinhole diameter could be minimized by reducing the overall path lengths of the instrument. This could be done, without any adverse effect on instrument resolution, by reducing the spacing between optical elements.

The profile of the OI 1304 Å emission was modeled on the personal computer using the method of Gladstone (1992). The resulting profile was simulated on the DART program and interference runs were conducted. Fourier transform techniques were used to determine the feasibility of retrieving meaningful data from the instrument. It was found that the tuned frequency of the AMI should be offset approximately half the bandwidth of the instrument from the wavelength of interest. This places the profile in the center of the resulting wavelength spectrum. This was effectively demonstrated by modeling a scaled emission line profile offset from  $\lambda_0$ . This profile was accurately retrieved by taking the fourier transform of the interference profile obtained from the AMI. Finally, the suspected factor-of-two error in the DART application was confirmed by examination of the pixel spacing of the instrument.

The results presented herein have validated the overall design concept of the Plane Grating All-reflection Michelson Interferometer as a viable means of examining atomic oxygen emission line profiles. It is believed that with further development, this instrument has potential to play an important role in determining atomic oxygen distributions in the atmosphere and to become a catalyst in the further understanding of the physics of the atmosphere.

## **B. RECOMMENDATIONS FOR FURTHER STUDY**

The research presented in this thesis was conducted using purely simulation and modeling techniques on the personal computer. Further work must now be done to build

and test a working prototype of this instrument in the visible and ultraviolet regions of the electromagnetic spectrum, continuing on the work performed in the laboratory by Wallace (1992) and Risley (1993). Of particular interest is experimentation with shorter coherence length sources and the testing of the fourier transform techniques used here on actual experimental data.

Further work in the simulation area includes revising the DART application to ensure that a significantly large number of wavelengths may be entered at the DART aperture. A revision to allow the user to select the number of bins under which the interference data is summed is also required. By so doing, equivalent resolutions can be achieved by simulation and by experimentation using a 1024 pixel detector. Additional work in the immediate area of this thesis can include: (1) devising a method for calculating and then removing the increase in intensity of the data with x-axis position caused by the off-axis parabola; (2) designing an AMI that is tuned to a wavelength offset from the desired  $\lambda_0$  so that wavelengths on either side of  $\lambda_0$  can be distinguished, providing a two-sided representation of the line profile of interest; (3) investigating the source and removal of low frequency contamination in wavelength spectra; (4) continuing the examination of the effects on instrument resolution from pinhole sources and slits at the aperture; (5) redesigning the instrument to reduce the spacing between optical elements and therefore minimize the detrimental effects of pinhole size on fringe contrast; and (6) designing the entrance optics to narrow the bandwidth of the light incident on the AMI's grating so that the numerous orders caused by the continuum of wavelengths at the instrument's entrance slit will not unintentionally strike the detector and corrupt the data obtained.

## APPENDIX A

### IDL FUNCTION AND PROCEDURE LISTINGS

#### IDL Function MODEL1.PRO

This function provides the equation used to model the 1304 Å line profile.

```
FUNCTION MODEL1,FLUX,LDIS,LOFF,L0,L
  C=2.998E8
  LEFT=FLUX/(2*SQRT(1PI)*((C*LDIS/L0)-C))
  RIGHT=EXP(-(L-LOFF)/(LDIS-L0)^2)+EXP(-(L-(2*L0)+LOFF)/(LDIS-L0))^2)
RETURN,(LEFT*RIGHT)
END
```

#### IDL Procedure PROF.PRO

:A program to plot the oxygen 1304 Å line profile to screen

```
@MODEL1
FLUX=3830.0
XDIS=10.6 ;IN KM/SEC
XOFF=9.5 ;IN KM/SEC
LAMBDACTR=1304.0 ;IN ANGSTROMS
NUMPOINTS=40 ;RESOLUTION IS WIDTH/NUMPOINTS
WIDTH=2.0E-10 ;BANDWIDTH IN METERS
C=2.998E8 ;IN M/S

LAMBDA0=LAMBDACTR*1.E-10 ;LAMBDA IN METERS
XDIS=XDIS*1000 ;GIVES X's IN METERS/SEC
XOFF=XOFF*1000

LAMBDA0=(XDIS+C)*LAMBDA0/C
LAMBDAOFF=(XOFF+C)*LAMBDA0/C
HALFWIDTH=WIDTH/2.0
LAMBDA=FLTARR(NUMPOINTS)
PROFILE=FLTARR(NUMPOINTS)
LAMBDA=((FINDGEN(NUMPOINTS)*WIDTH/NUMPOINTS)+LAMBDA0-HALFWIDTH)
PROFILE=MODEL1(FLUX,LAMBDA0,LAMBDAOFF,LAMBDA0,LAMBDA)

PLOT,LAMBDA*1.E10,PROFILE,XRANGE=[1303.5,1304.5],BACK=255,COLOR=0,$
  TITLE='SOLAR OXYGEN 1304 ANGSTROM TRIPLET LINE PROFILE',$
  XTITLE='WAVELENGTH (ANGSTROMS)', $
  YTITLE='COUNT RATE (COUNTS/S/MILLIANGSTROM)'
END
```

## IDL Procedure PROFFIL.PRO

:A program to write the oxygen 1304 Å profile data to a file for inclusion later in a DART parameter file

```
@MODEL1
FLUX=3830.0
XDIS=10.6 ;IN KM/SEC
XOFF=9.5 ;IN KM/SEC
LAMBDACTR=1304.0 ;IN ANGSTROMS
NUMPOINTS=40 ;RESOLUTION IS WIDTH/NUMPOINTS
WIDTH=0.3E-10 ;BANDWIDTH IN METERS
C=2.998E8 ;IN M/S

LAMBDA0=LAMBDACTR*1.E-10 ;LAMBDA IN METERS
XDIS=XDIS*1000 ;GIVES X's IN METERS/SEC
XOFF=XOFF*1000

LAMBDA0=(XDIS+C)*LAMBDA0/C
LAMBDAOFF=(XOFF+C)*LAMBDA0/C
HALFWIDTH=WIDTH/2.0
LAMBDA=FLTARR(NUMPOINTS)
PROFILE=FLTARR(NUMPOINTS)
LAMBDA=(FINDGEN(NUMPOINTS)*WIDTH/NUMPOINTS)+LAMBDA0-HALFWIDTH)
PROFILE=MODEL1(FLUX,LAMBDA0,LAMBDAOFF,LAMBDA0,LAMBDA)
PROFILE2=FIX(PROFILE*1000.)
OPENW,1,'OXYGEN.DAT'
FOR J=0,NUMPOINTS-1 DO PRINTF,1,FORMAT='(I,F10.4)',PROFILE2(J),LAMBDA(J)*1.E10
CLOSE,1
END
```



## IDL Procedure PROFPRT.PRO

;Procedure to plot the Oxygen 1304 Å line profile to a postscript file for printing as a figure

```
@MODEL1
FLUX=3830.0
XDIS=10.6                ;IN KM/SEC
XOFF=9.5                 ;IN KM/SEC
LAMBDACTR=1304.0        ;IN ANGSTROMS
NUMPOINTS=39            ;RESOLUTION IS WIDTH/NUMPOINTS
WIDTH=2.0E-10           ;BANDWIDTH IN METERS
C=2.998E8               ;IN M/S

LAMBDA0=LAMBDACTR*1.E-10 ;LAMBDA IN METERS
XDIS=XDIS*1000          ;GIVES X's IN METERS/SEC
XOFF=XOFF*1000

LAMBDA0=C/LAMBDACTR
LAMBDA0OFF=XOFF+C
HALFWIDTH=WIDTH/2.0
LAMBDA=FLTARR(NUMPOINTS)
PROFILE=FLTARR(NUMPOINTS)
LAMBDA=((FINDGEN(NUMPOINTS)*WIDTH/NUMPOINTS)+LAMBDA0-HALFWIDTH)
PROFILE=MODEL1(FLUX,LAMBDA0,LAMBDA0OFF,LAMBDA0,LAMBDA)

SET_PLOT,'PS'
DEVICE,FILENAME='FIGURE.PS',/INCHES,/PORTRAIT,SCALE=.72
PLOT,LAMBDA*1.E10,PROFILE,XRANGE=[1303.5,1304.5],BACK=255,COLOR=0,$
  TITLE='SOLAR OXYGEN 1304 ANGSTROM TRIPLET LINE PROFILE',$
  XTITLE='WAVELENGTH (ANGSTROMS)', $
  YTITLE='COUNT RATE (COUNTS/S/MILLIANGSTROM) '
DEVICE,/CLOSE
SET_PLOT,'WIN'
END
```

## IDL Procedure INPLOT.PRO

```
;This is an IDL procedure that will read a file produced by DART
;   consisting of 400 vertical bins of interference intensities
;   along the x direction, plot the resulting data, take a fourier
;   transform of the figure, then plot the results all to the screen.

XAX=FLTARR(400)           ;PLOT X-AXIS DATA ARRAY
XPOS=FLTARR(400)         ;POSITION ALONG DETECTOR X-AXIS
INTEN=FLTARR(400)        ;INTENSITY (Y-AXIS) ARRAY
PEAKS=0
JUNK=STRING(0)
FILENAME=STRING(0)
PRINT,'ENTER THE NAME OF THE INTERFERENCE FILE '
READ,FILENAME
OPENR,1,FILENAME
READF,1,JUNK              ;USE UP 'DART INTERFERENCE FILE' TEXT
FOR I=0,399 DO BEGIN
    READF,1,X,Y
    XPOS(I)=X
    INTEN(I)=Y
ENDFOR
CLOSE,1
XMAX=MAX(XPOS)
XMIN=MIN(XPOS)

;SUBTRACT THE AVERAGE VALUE FROM THE INTENSITY
;ARRAY TO MAKE IT SYMMETRIC ABOUT THE X AXIS.
INTEN=INTEN-(TOTAL(INTEN)/400.)
;USE 'REVERSE' IF PLOTTING LEFT SIDE OF LAMBDA 0
;USE REGULAR XAX IF PLOTTING RIGHT SIDE OF LAMBDA 0
;XAX=REVERSE(1304.-(.00207*FINDGEN(200)))
XAX=1304.+(.00207*FINDGEN(200))

PLOT,XPOS,INTEN,XRANGE=[XMIN,XMAX],BACK=255,COLOR=1,$
TITLE='INTERFERENCE PATTERN',XTITLE='Position on Detector (cm)',$
YTITLE='Relative Intensity'

;THE FOLLOWING SECTION NOT USED IN FINAL PRODUCT BUT ALLOWS
;USER TO EXAMINE THE FIRST PLOT BEFORE CALLING UP THE SECOND
PRINT,'ENTER THE NUMBER OF FRINGES (PEAKS)'
READ,PEAKS
;L=(XMAX-XMIN)/PEAKS)/100.
;DELLAMBDA=(1304.E-10/(2.*L))*SQRT((1./(6.E6))^2-(1304.E-10/2.)^2)
;PRINT,DELLAMBDA*1.E10,'ANGSTROMS'

FORT=ABS(FFT(INTEN,-1))   ;FAST FOURIER TRANSFORM
PLOT,XAX,FORT(0:199),BACK=255,COLOR=1,TITLE='FREQUENCY SPECTRUM',$
XTITLE='Wavelength (Angstroms)',YTITLE='Relative Intensity',$
XRANGE=[1304.0,1304.4]

END
```

## IDL Procedure INPRT.PRO

This procedure plots the interference profile and the FFT to a postscript file but doesn't subtract off the average intensity to remove the unwanted DC component nor does it scale the wavelength axis. The FFT plots produced here are double sided.

```
;This is an IDL program that will read a file produced by DART
;   consisting of 400 bins of interference intensities summed
;   along the y direction, plot the resulting data, take a fourier
;   transform, then plot the results all to a postscript file.
```

```
XPOS=FLTARR(400)
INTEN=FLTARR(400)
JUNK=STRING(0)
FILENAME=STRING(0)
PRINT,'ENTER THE NAME OF THE INTERFERENCE FILE '
READ,FILENAME
OPENR,1,FILENAME
READF,1,JUNK                ;USE UP 'DART INTERFERENCE FILE' TEXT
FOR I=0,399 DO BEGIN
    READF,1,X,Y
    XPOS(I)=X
    INTEN(I)=Y
ENDFOR
CLOSE,1
XMAX=MAX(XPOS)
XMIN=MIN(XPOS)
SET_PLOT,'PS'
DEVICE,FILENAME='FIG2.PS',/INCHES,/PORTRAIT,SCALE=.72

PLOT,XPOS,INTEN,XRANGE=[-2.,2.],BACK=255,COLOR=1,$
    TTITLE=' INTENSITY VS. DETECTOR X POSITION',$
    XTITLE='Detector X Position (cm)',YTITLE='Relative Intensity'

FORT=ABS(FFT(INTEN,-1))
PLOT,FORT,BACK=255,COLOR=1,TTITLE=' FOURIER TRANSFORM PLOT',$
    XTITLE=' FFT Solution Array Element Number',YTITLE='Relative Intensity',$
    XRANGE=[0.00,400]

PLOT,FORT,BACK=255,COLOR=1,TTITLE='IDEAL PS FFT PLOT',$
    XTITLE=' FFT Solution Array Position',YTITLE='Relative Intensity',$
    XRANGE=[180,200]

DEVICE,/CLOSE
SET_PLOT,'WIN'
END
```

## IDL Procedure IPRT.PRO

This procedure plots the interference profile and the FFT to a postscript file and then subtracts off the average intensity to remove the unwanted DC component. It also introduces the wavelength axis calibration and plots the wavelength spectrum.

```
;This is an IDL program that will read a file produced by DART
;   consisting of 400 bins of interference intensities summed
;   along the y direction, plot the resulting data, take a fourier
;   transform , then plot the results all to a postscript file.
XAX=FLTARR(400)
XPOS=FLTARR(400)
INTEN=FLTARR(400)
JUNK=STRING(0)
FILENAME=STRING(0)
PRINT,'ENTER THE NAME OF THE INTERFERENCE FILE '
READ,FILENAME
OPENR,1,FILENAME
READF,1,JUNK                               ;USE UP 'DART INTERFERENCE FILE' TEXT
FOR I=0,399 DO BEGIN
    READF,1,X,Y
    XPOS(I)=X
    INTEN(I)=Y
ENDFOR
CLOSE,1
XMAX=MAX(XPOS)
XMIN=MIN(XPOS)
SET_PLOT,'PS'
DEVICE,FILENAME='t7.PS',/INCHES,/PORTRAIT,scale=.72

INTEN=INTEN-(TOTAL(INTEN)/400.)
;XAX=1304.+(.00207*FINDGEN(200))
XAX=REVERSE(1304.-(.00207*FINDGEN(200)))

PLOT,XPOS,INTEN,XRANGE=[-2.,2.],BACK=255,COLOR=1,$
    TITLE=' INTENSITY VS. DETECTOR X POSITION',$
    XTITLE='Detector X Position (cm)',YTITLE='Relative Intensity'

FORT=ABS(FFT(INTEN,-1))
PLOT,XAX,FORT(200:*),BACK=255,COLOR=1,TITLE=' FFT PLOT',$
    XTITLE='Wavelength (Angstroms)',YTITLE='Relative Intensity',$
    XRANGE=[1303.6,1304.0]

PLOT,XAX,FORT(200:*),BACK=255,COLOR=1,TITLE=' FFT PLOT',$
    XTITLE='Wavelength (Angstroms)',YTITLE='Relative Intensity',$
    XRANGE=[1303.75,1303.85]

DEVICE,/CLOSE
SET_PLOT,'WIN'
END
```

## APPENDIX B

### DART PARAMETER FILES

#### Parameter File 0ORDER.TXT

This file contains the parameters for a typical run for the zero order path of the original interferometer.

04/16/1993 18:13:06

The analysis wavelength is 1304.0001 angstroms.

#### Aperture data:

Center of Opening (x,y,z): [ 0.00000, 0.00000, 0.00000]

Aperture dimensions (x,y): [ 2.50000, 2.50000]

Points across opening (x,y): [ 10, 10]

Angular beam spread (x,y): [ 0.000, 0.000]

Number of angles in spread (x,y): [ 1, 1]

Center angle of beam rays (x,y): [ 0.000, 0.000]

No offset angles are traced.

Aperture shape is rectangular.

Beam spread shape is rectangular.

#### There are 4 elements:

x y z

The Center of Element 1 coordinate System is 0.000000 0.000000 40.000000

Euler Angles in Degrees: 0.000000 147.000000 0.000000

Plane Grating with 60000.000 grooves per cm and order 0.

Element mask is rectangular with width 5.000 and height 5.000 cm.

x y z

The Center of Element 2 coordinate System is 18.271000 0.000000 31.865000

Euler Angles in Degrees: 0.000000 -66.000000 0.000000

Plane Mirror

Element mask is circular with width 5.000 and height 5.000 cm.

x y z

The Center of Element 3 coordinate System is 0.000000 0.000000 40.000000

Euler Angles in Degrees: 0.000000 147.000000 0.000000

Plane Grating with 60000.000 grooves per cm and order 1.

Element mask is rectangular with width 5.000 and height 5.000 cm.

x y z  
The Center of Element 4 coordinate System is 18.211000 0.000000 22.872000  
Euler Angles in Degrees: 0.000000 313.246000 0.000000  
Plane Surface  
Element mask is rectangular with width 5.000 and height 5.000 cm.

There were 100 rays from all points and angles.  
100 rays hit the detector.  
0 failed to hit first element.  
0 were stopped after the first.

### Parameter File -1ORDER.TXT

This file contains the parameters for a typical run for the minus first order path of the original interferometer.

03/22/1993 11:04:47

The analysis wavelength is 1305.0000 angstroms.

Aperture data:  
Center of Opening (x,y,z): [ 0.00000, 0.00000, 0.00000]  
Aperture dimensions (x,y): [ 2.50000, 2.50000]  
Points across opening (x,y): [ 100, 100]  
Angular beam spread (x,y): [ 0.000, 0.000]  
Number of angles in spread (x,y): [ 1, 1]  
Center angle of beam rays (x,y): [ 0.000, 0.000]  
No offset angles are traced.  
Aperture shape is rectangular.  
Beam spread shape is rectangular.

There are 4 elements:

x y z  
The Center of Element 1 coordinate System is 0.000000 0.000000 40.000000  
Euler Angles in Degrees: 0.000000 147.000000 0.000000  
Plane Grating with 60000.000 grooves per cm and order -1.  
Element mask is rectangular with width 5.000 and height 5.000 cm.

x y z  
The Center of Element 2 coordinate System is 6.592000 0.000000 21.118000  
Euler Angles in Degrees: 0.000000 340.754000 0.000000  
Plane Mirror  
Element mask is circular with width 5.000 and height 5.000 cm.

x y z  
The Center of Element 3 coordinate System is 0.000000 0.000000 40.000000  
Euler Angles in Degrees: 0.000000 147.000000 0.000000  
Plane Grating with 60000.000 grooves per cm and order 0.  
Element mask is rectangular with width 5.000 and height 5.000 cm.

**x y z**

**The Center of Element 4 coordinate System is 18.211000 0.000000 22.872000**

**Euler Angles in Degrees: 0.000000 313.246000 0.000000**

**Plane Surface**

**Element mask is rectangular with width 5.000 and height 5.000 cm.**

**Parameter file PAR4.TXT**

**This file contains the off-axis parabolic reflector element.**

**06/03/1993 18:27:20**

**The analysis wavelength is 5000.0000 angstroms.**

**Aperture data:**

**Center of Opening (x,y,z): [ 0.00000, 0.00000, 0.00000]**

**Aperture dimensions (x,y): [ 0.01000, 0.01000]**

**Points across opening (x,y): [ 1, 1]**

**Angular beam spread (x,y): [ 45.000, 45.000]**

**Number of angles in spread (x,y): [ 10, 10]**

**Center angle of beam rays (x,y): [ 5.000, 0.000]**

**No offset angles are traced.**

**Aperture is adjusted to an elliptical shape.**

**Beam spread shape is rectangular.**

**There are 3 elements:**

**x y z**

**The Center of Element 1 coordinate System is -5.970000 0.000000 0.000000**

**Euler Angles in Degrees: 0.000000 90.000000 0.000000**

**Concave Parabolic Mirror with x-axis focal length = 5.970 and y-axis focal length = 5.970**

**Element mask is circular with width 31.000 and height 31.000 cm.**

**x y z**

**The Center of Element 2 coordinate System is 5.000000 0.000000 11.940000**

**Euler Angles in Degrees: 0.000000 90.000000 0.000000**

**Plane Surface**

**Element mask is circular with width 6.350 and height 6.350 cm.**

**x y z**

**The Center of Element 3 coordinate System is 20.000000 0.000000 10.000000**

**Euler Angles in Degrees: 0.000000 90.000000 0.000000**

**Plane Surface**

**Element mask is circular with width 20.000 and height 20.000 cm.**

**There were 100 rays from all points and angles.**

**27 rays hit the detector.**

**34 failed to hit first element.**

**39 were stopped after the first.**



## Parameter file IPS0.TXT

This file describes the zero order path of the entire All-reflection Michelson Interferometer as simulated in this thesis.

05/12/1993 09:14:02

The analysis wavelength is 1303.6500 angstroms.

### Aperture data:

Center of Opening (x,y,z): [ 0.00000, 0.00000, 0.00000]

Aperture dimensions (x,y): [ 0.00000, 0.00000]

Points across opening (x,y): [ 1, 1]

Angular beam spread (x,y): [ 12.000, 12.000]

Number of angles in spread (x,y): [ 4, 4]

Center angle of beam rays (x,y): [ -1.000, 0.000]

No offset angles are traced.

Aperture is adjusted to an elliptical shape.

Beam spread is adjusted to an elliptical shape.

There are 6 elements:

x y z

The Center of Element 1 coordinate System is -5.970000 0.000000 0.000000

Euler Angles in Degrees: 0.000000 90.000000 0.000000

Concave Parabolic Mirror with x-axis focal length = 5.970 and y-axis focal length = 5.970

Element mask is circular with width 31.000 and height 31.000 cm.

x y z

The Center of Element 2 coordinate System is 5.000000 0.000000 11.940000

Euler Angles in Degrees: 0.000000 90.000000 0.000000

Plane Surface

Element mask is circular with width 6.350 and height 6.350 cm.

x y z

The Center of Element 3 coordinate System is 60.000000 0.000000 11.940000

Euler Angles in Degrees: 0.000000 237.000000 0.000000

Plane Grating with 60000.000 grooves per cm and order 0.

Element mask is rectangular with width 5.000 and height 5.000 cm.

x y z

The Center of Element 4 coordinate System is 51.865270 0.000000 -6.330910

Euler Angles in Degrees: 0.000000 24.000000 0.000000

Plane Mirror

Element mask is circular with width 5.000 and height 5.000 cm.

x y z

The Center of Element 5 coordinate System is 60.000000 0.000000 11.940000

Euler Angles in Degrees: 0.000000 237.000000 0.000000

Plane Grating with 60000.000 grooves per cm and order 1.

Element mask is rectangular with width 5.000 and height 5.000 cm.

x y z

The Center of Element 6 coordinate System is 42.872000 0.000000 -6.271000

Euler Angles in Degrees: 0.000000 43.245570 0.000000

Plane Surface

Element mask is rectangular with width 2.500 and height 1.000 cm.

There were 12 rays from all points and angles.

2 rays hit the detector.

0 failed to hit first element.

10 were stopped after the first.

### Parameter file IPS-1.TXT

This file describes the minus first order path of the entire All-reflection Michelson Interferometer as simulated in this thesis.

05/26/1993 15:32:58

Ideal Point Source - Tuned to 1304.000 Angstroms -1 order path

The analysis wavelength is 1303.6500 angstroms.

Aperture data:

Center of Opening (x,y,z): [ 0.00000, 0.00000, 0.00000]

Aperture dimensions (x,y): [ 0.00000, 0.00000]

Points across opening (x,y): [ 1, 1]

Angular beam spread (x,y): [ 12.000, 12.000]

Number of angles in spread (x,y): [ 5, 5]

Center angle of beam rays (x,y): [ -1.000, 0.000]

No offset angles are traced.

Aperture is adjusted to an elliptical shape.

Beam spread is adjusted to an elliptical shape.

There are 6 elements:

x y z

The Center of Element 1 coordinate System is -5.970000 0.000000 0.000000

Euler Angles in Degrees: 0.000000 90.000000 0.000000

Concave Parabolic Mirror with x-axis focal length = 5.970 and y-axis focal length = 5.970

Element mask is circular with width 31.000 and height 31.000 cm.

x y z

The Center of Element 2 coordinate System is 5.000000 0.000000 11.940000

Euler Angles in Degrees: 0.000000 90.000000 0.000000

Plane Surface

Element mask is circular with width 6.350 and height 6.350 cm.

x y z

The Center of Element 3 coordinate System is 60.000000 0.000000 11.940000

Euler Angles in Degrees: 0.000000 237.000000 0.000000

Plane Grating with 60000.000 grooves per cm and order -1.

Element mask is rectangular with width 5.000 and height 5.000 cm.

x y z

The Center of Element 4 coordinate System is 41.117710 0.000000 5.347650

Euler Angles in Degrees: 0.000000 70.754430 0.000000

Plane Mirror

Element mask is circular with width 5.000 and height 5.000 cm.

x y z

The Center of Element 5 coordinate System is 60.000000 0.000000 11.940000

Euler Angles in Degrees: 0.000000 237.000000 0.000000

Plane Grating with 60000.000 grooves per cm and order 0.

Element mask is rectangular with width 5.000 and height 5.000 cm.

x y z

The Center of Element 6 coordinate System is 42.872000 0.000000 -6.271000

Euler Angles in Degrees: 0.000000 43.245570 0.000000

Plane Surface

Element mask is rectangular with width 2.500 and height 1.000 cm.

There were 23 rays from all points and angles.

6 rays hit the detector.

0 failed to hit first element.

17 were stopped after the first.

## LIST OF REFERENCES

- Atkinson, J. D., *Implementation and Use of a Computational Ray-Tracing Program for the Design and Analysis of Complex Optical Systems*, Master's Thesis, Naval Postgraduate School, Monterey, California, March 1993.
- Cleary, D. D., Nichols, J. W., and Davis, D. S., "Design for an All-reflection Michelson Interferometer", *Applied Optics*, 31, 433, 1992.
- Cleary, D. D., Wallace, K. M., Atkinson, J. D., Carlson, S. M., and Risley, A. D., "An All-Reflection Michelson Interferometer for Solar Occultation Measurements of the O<sub>I</sub> 1304-Å Emission", paper to be submitted to *Applied Optics—Technical Notes*, 1993.
- Gladstone, G. R., "Solar O<sub>I</sub> 1304 Å Triplet Line Profiles", *Journal of Geophysical Research*, v. 97, pp. 19519-19525, 1 December 1992.
- Nichols, J., *The Design of a New Far Ultraviolet Interferometer for Ionospheric Spectroscopy*, Master's Thesis, Naval Postgraduate School, Monterey, California, December 1990.
- Pedrotti, F. L., and Pedrotti, L. S., *Introduction to Optics*, Prentice-Hall, Inc., 1987.
- Risley, A. D., *Developmental Testing of a Prototype All-Reflection Michelson Interferometer*, Master's Thesis, Naval Postgraduate School, Monterey, California, June 1993.
- Tascione, T. F., *Introduction to the Space Environment*, Orbit Book Company, 1988.
- Wallace, K. M., *Design of a High Resolution Spatial Heterodyne Interferometer*, Master's Thesis, Naval Postgraduate School, Monterey, California, December 1992.

## INITIAL DISTRIBUTION LIST

1. Defense Technical Information Center 2  
Cameron Station  
Alexandria, Virginia 22304-6145
2. Library, Code 52 2  
Naval Postgraduate School  
Monterey, California 93943-5002
3. Dr. K. E. Woehler, Chairman PH 1  
Physics Department  
Naval Postgraduate School  
Monterey, California 93943-5000
4. Dr. David D. Cleary 3  
Physics Department, PH-CL  
Naval Postgraduate School  
Monterey, California 93943-5000
5. LT Scott M. Carlson 2  
8623 Darien Court  
Annandale, Virginia 22003
6. Dr. Larry Paxton 1  
Mail Stop 24-E115  
Johns Hopkins University  
Applied Physics Laboratory  
Johns Hopkins Road  
Laurel, Maryland 20723-6099